



# Preparation of porous $\alpha$ -Fe<sub>2</sub>O<sub>3</sub> thin films for efficient photoelectrocatalytic degradation of basic blue 41 dye

Manel Machreki<sup>a</sup>, Takwa Chouki<sup>a</sup>, Mitja Martelanc<sup>b</sup>, Lorena Butinar<sup>b</sup>,  
Branka Mozetič Vodopivec<sup>b</sup>, Saim Emin<sup>a,\*</sup>

<sup>a</sup> Materials Research Laboratory, University of Nova Gorica, Vipavska 11c, 5270 Ajdovščina, Slovenia

<sup>b</sup> Wine Research Centre, University of Nova Gorica, Glavni Trg 8, 5271 Vipava, Slovenia

## ARTICLE INFO

Editor: Dr. G. Palmisano

### Keywords:

$\alpha$ -Fe<sub>2</sub>O<sub>3</sub> thin films  
Photoelectrocatalysis  
Kinetics  
Visible light  
Degradation  
Textile dye

## ABSTRACT

A novel method was developed for the preparation of porous hematite ( $\alpha$ -Fe<sub>2</sub>O<sub>3</sub>) thin films. First, a solution containing iron precursor was spin-coated on fluorine-doped tin oxide substrate and later short heat-treated at 750 °C. The prepared  $\alpha$ -Fe<sub>2</sub>O<sub>3</sub> thin films were applied as dual-function catalyst in photoelectrochemical (PEC) water oxidation and textile dye degradation studies. For the first time,  $\alpha$ -Fe<sub>2</sub>O<sub>3</sub> thin films were used in efficient PEC degradation of a textile dye (Basic Blue 41 – B41) using in-situ generated reactive chlorine species. In comparison with photocatalytic and electrocatalytic approaches, the PEC technique allows faster degradation of B41 dye at an applied bias potential of 1.5 V versus reversible hydrogen electrode and under visible light illumination. In the presence of Cl<sup>−</sup> using the PEC approach the degradation of B41 reaches 99.8%. High-performance liquid chromatography coupled with UV–VIS system confirmed the degradation of B41 dye using PEC. Gas-chromatography coupled to mass spectrometry was used to study the by-products obtained during PEC degradation. Chemical oxygen demand analyses confirmed that the mineralization level of B41 is in the order of 68%. The  $\alpha$ -Fe<sub>2</sub>O<sub>3</sub> films developed in this study give a higher level of PEC degradation efficiency compared to other iron oxide-based systems.

## 1. Introduction

The photoelectrochemical (PEC) approach has emerged as a promising advanced oxidation process to eliminate a broad range of organic contaminants from wastewaters and indoor air [1,2]. The synergistic effect of electro- and photocatalytic processes in PEC has been shown to yield excellent performance for organic pollutant degradation [3,4]. It has been demonstrated that oxidation of organics using PEC can proceed via direct or indirect mechanisms [5]. The direct oxidation occurs with electron transfer between the organic molecules and the electrode. On the other side, the indirect oxidation involves strong oxidant species such as reactive chlorine species (RCS), hydroxyl radicals ( $\bullet$ OH), hydrogen peroxide (H<sub>2</sub>O<sub>2</sub>), or sulfate radicals (SO<sub>4</sub><sup>•−</sup>) [1]. Especially, indirect electro-oxidation using RCS such as chlorine radicals (Cl $\bullet$ , Cl<sub>2</sub><sup>•−</sup>), chlorine (Cl<sub>2</sub>), hypochlorite ion (ClO<sup>−</sup>), and hypochlorous acid (HOCl) showed as an efficient species for degradation of alcohols and carboxylic acids [6]. The most common source of Cl<sup>−</sup> ions include an electrolyte such as sodium chloride (NaCl). It is well-known that the Cl<sup>−</sup>

ions oxidation using the electrocatalytic (EC) or PEC approach yields Cl<sub>2</sub> gas. Depending on the solution pH, the obtained Cl<sub>2</sub> may be stable under acidic condition (pH < 3.3), hydrolyze to either HOCl (3.3 < pH < 7.5) or ClO<sup>−</sup> ion (pH > 7.5) [7]. The relative oxidation power of HOCl is 80 times higher than that of ClO<sup>−</sup> and usually, PEC oxidation is more efficient in an acidic medium [8,9].

Titanium dioxide (TiO<sub>2</sub>), as one of the most studied semiconductors in PEC studies, has been applied for degradation of various contaminants such as sulfamethoxazole, fulvic acid, sodium *p*-cuenesulfonate, etc [10–13]. However, the large band-gap of TiO<sub>2</sub> (~3.2 eV) limits its light-harvesting ability only in the UV region [14]. In this context, researchers have focused on semiconductor materials such as tungsten trioxide (WO<sub>3</sub>), bismuth vanadate (BiVO<sub>4</sub>), or Fe<sub>2</sub>O<sub>3</sub>, which absorb in the visible range [15]. Koo et al. demonstrated that WO<sub>3</sub> with a band-gap of ~2.8 eV prepared by electrodeposition is efficient for PEC degradation of organics using in-situ generated RCS [7]. Other semiconductors that possess a small band-gap include  $\alpha$ -Fe<sub>2</sub>O<sub>3</sub> (~2.1 eV). The use of  $\alpha$ -Fe<sub>2</sub>O<sub>3</sub> in PEC degradation of organics is mainly limited to

\* Corresponding author.

E-mail address: [saim.emin@ung.si](mailto:saim.emin@ung.si) (S. Emin).

<https://doi.org/10.1016/j.jece.2021.105495>

Received 25 January 2021; Received in revised form 8 April 2021; Accepted 11 April 2021

Available online 14 April 2021

2213-3437/© 2021 Elsevier Ltd. All rights reserved.

$\text{Na}_2\text{SO}_4$  and  $\text{HClO}_4$  electrolytes. Zhang et al. have used  $\alpha\text{-Fe}_2\text{O}_3$  films for PEC degradation of methyl orange and p-nitrophenol in  $\text{Na}_2\text{SO}_4$  electrolyte [16]. In the presence of  $\text{Na}_2\text{SO}_4$  electrolytes and after applying sufficient voltage PEC produces reactive  $\text{SO}_4^{\bullet-}$  radicals that take part in organics degradation [11]. Other reports where the main oxidant is the  $\text{SO}_4^{\bullet-}$  radical include  $\alpha\text{-Fe}_2\text{O}_3$  thin films for degradation of methylene blue (MB) [17,18] or composites made of  $\alpha\text{-Fe}_2\text{O}_3/\text{ZnO}$  for removal of 4-chlorophenol [19] and  $\alpha\text{-Fe}_2\text{O}_3/\text{Cu}_2\text{O}$  for degradation of oxytetracycline [20]. In similar ways, Suryavanshi et al. and Mahadik et al. have used  $\alpha\text{-Fe}_2\text{O}_3$  thin films to degrade MB and rhodamine B dyes in  $\text{HClO}_4$  electrolyte [21,22]. To the best of author's knowledge, in the case of  $\alpha\text{-Fe}_2\text{O}_3$  PEC systems the main oxidants are in-situ generated  $\text{SO}_4^{\bullet-}$  and  $\bullet\text{OH}$  radicals [23]. However, standard potentials for the generation of  $\bullet\text{OH}$  (2.80 V vs. NHE) and  $\text{SO}_4^{\bullet-}$  (2.60 V vs. NHE) are quite high, and their use presents a drawback in PEC oxidation of organics [11].

$\alpha\text{-Fe}_2\text{O}_3$  is considered a promising material for PEC wastewater treatment because it is earth-abundant, non-toxic, and exhibits a small band-gap [24]. Besides its several advantages,  $\text{Fe}_2\text{O}_3$  suffers from low absorption coefficient, low carrier mobility ( $<1\text{ cm}^2\text{ V}^{-1}\text{ s}^{-1}$ ), short hole diffusion length (2–4 nm), and shorter excited state lifetime ( $\sim 10\text{ ps}$ ) [25]. To overcome these limitations, various strategies are employed, such as doping with various elements ( $\text{Ti}^{4+}$ ,  $\text{Pt}^{4+}$ , or  $\text{Sn}^{4+}$ ) or the use of nanoparticles are convenient ways to achieve an enhancement in photocurrent response [26–28]. The approaches used for preparation of  $\alpha\text{-Fe}_2\text{O}_3$  thin films include hydrothermal [29], electrodeposition [30], sol-gel [31], atomic layer deposition (ALD) [32], chemical vapor deposition (CVD) [33,34], etc. One very common technique for the growth of  $\text{Fe}_2\text{O}_3$  thin film is the CVD approach. This process involves the reaction of precursors in the vapor phase within a deposition chamber on a substrate surface [35]. In this way, the obtained films are typically non-conformal and granular [36,37]. On the other side, ALD produces very uniform  $\text{Fe}_2\text{O}_3$  thin films and allows precise control over the thickness of the films. However, this technique usually uses expensive precursors like bis(2,4-methylpentadienyl) iron (II) [38], bis(N, N'-di-*t*-butylacetamidinato)iron(II) [32], tris(2,2,6,6-tetramethyl-3, 5-heptanedionate) iron (III) [39], etc. Another drawback for ALD is the slow growth rate of materials [40]. Hydrothermal technique can grow directly thin films on substrates [41]. However, the small sizes of the vessels often used can be a limitation to grow large area metal oxide thin films. Therefore, it is important to employ an approach that avoids the use of expensive chemicals and apparatuses, toxic precursors, high vacuum systems, etc [42].

This study proposes a novel method for preparation of photoactive  $\alpha\text{-Fe}_2\text{O}_3$  thin films using spin-coating of iron precursors on fluorine-doped tin oxide ( $\text{F:SnO}_2$ , FTO) substrates. The approach includes a short heat treatment step at  $750^\circ\text{C}$ . The advantage of spin-coating is the simplicity of the procedure, which allows getting uniform coatings with defined thicknesses [43,44]. For the first time,  $\alpha\text{-Fe}_2\text{O}_3$  films were used in PEC degradation of a model B41 dye contaminant where the oxidative species include in-situ generated RCS. Reusability tests confirmed that the  $\alpha\text{-Fe}_2\text{O}_3$  films are stable and efficient during the degradation of the B41 dye. The selection of B41 dye was due the fact that it is a harmful effluent in the textiles industry [45]. High performance liquid chromatography coupled with UV–VIS detection (HPLC-UV/VIS) and gas chromatography-mass spectrometry (GC-MS) were used to monitor the degradation of B41 dye and to evaluate the by-products during degradation. Various operation parameters, including anodic potential, solution pH, electrolytes, and dye concentration, were investigated to determine the optimal conditions for B41 dye degradation.

## 2. Materials and methods

### 2.1. Chemicals and materials

2-methoxyethanol (99%), ethyl acetoacetate, tetrabutylammonium perchlorate, iron (III) nitrate nonahydrate ( $\text{Fe}(\text{NO}_3)_3 \cdot 9\text{H}_2\text{O}$ , 98%),

ethylenediaminetetraacetic acid (EDTA), Sodium thiosulfate ( $\text{Na}_2\text{S}_2\text{O}_3$ ), tert-butyl alcohol (TBA)), acetonitrile and methanol were purchased from Sigma-Aldrich. Polyvinylpyrrolidone (PVP, M.W. 55,000), sodium chloride (NaCl, 99%), sodium sulfate ( $\text{Na}_2\text{SO}_4$ , >99%), coumarin, sodium hypochlorite (NaOCl) and ferrocene (99%) were purchased from Alfa Aesar. Ammonium chloride ( $\text{NH}_4\text{Cl}$ , 98%) and 7-Hydroxycoumarin was obtained from Acros Organics. As a substrate was used an FTO on borosilicate glass (Solaronix, Swiss). A graphite block (99.9%) was purchased from Beijing Great Wall Co., Ltd. (China). Deionized water was used in all the experiments.

### 2.2. Preparation of a porous $\alpha\text{-Fe}_2\text{O}_3$ thin film

The  $\alpha\text{-Fe}_2\text{O}_3$  photoanode was prepared by spin-coating method. Firstly,  $7.7\text{ }\mu\text{mol}$  of PVP was dissolved in  $19.7\text{ mmol}$  2-methoxyethanol and  $7.7\text{ mmol}$  ethyl acetoacetate. Then,  $2.0\text{ mmol}$   $\text{Fe}(\text{NO}_3)_3 \cdot 9\text{H}_2\text{O}$  was added into the above solution and stirred vigorously for 30 min. The obtained solution was spin-coated at 1000 rpm on FTO substrate and calcined at  $750^\circ\text{C}$  for 10 min under air atmosphere. The heating rate was kept at  $8^\circ\text{C min}^{-1}$ . The choice of borosilicate glass was due to its high thermal stability (softening point  $>900^\circ\text{C}$ ).

### 2.3. Characterization of the $\alpha\text{-Fe}_2\text{O}_3$ thin film

X-ray diffraction (XRD) pattern of the  $\alpha\text{-Fe}_2\text{O}_3$  electrode was collected within the  $2\theta$  range from  $10^\circ$  to  $90^\circ$  with a constant step of  $0.03^\circ$  using MiniFlex 600 W (Rigaku) diffractometer with  $\text{Cu-K}\alpha$  radiation. Phase identification was performed with the PDXL software using the COD database. Diffuse reflectance spectrum is recorded on a Lambda 650 UV–VIS spectrophotometer (PerkinElmer). The morphology of the  $\alpha\text{-Fe}_2\text{O}_3$  was studied using a scanning electron microscope JSM 7100F SEM (JEOL) equipped with a field-emission electron gun and coupled to an energy dispersive X-ray spectrometer (EDS) (Oxford Instruments). Transmission electron microscopy (TEM) and Scanning-TEM (STEM) studies were carried out with a JEOL 2100F. EC and PEC measurements were done in a three-electrode system with a Cappuccino cell (Fig. S1). An O-ring was used to define the electrode area to  $0.283\text{ cm}^2$ . The potential of the working electrode was controlled by a potentiostat (EDAQ SP1). A graphite plate and a  $\text{Hg}/\text{Hg}_2\text{SO}_4$  electrode were used as the counter and reference electrodes, respectively. Experimentally measured potentials were converted to the reversible hydrogen electrode (RHE) scale using the Nernst equation:  $E_{\text{RHE}} = E_{\text{Hg}/\text{Hg}_2\text{SO}_4} + E_{\text{Hg}/\text{Hg}_2\text{SO}_4}^0 + 0.059 \times \text{pH}$ . In this equation,  $E_{\text{Hg}/\text{Hg}_2\text{SO}_4}$  was the measured potential against the  $\text{Hg}/\text{Hg}_2\text{SO}_4$  reference electrode and  $E_{\text{Hg}/\text{Hg}_2\text{SO}_4}^0$  was taken as  $0.65\text{ V}$  at  $25^\circ\text{C}$ . The electrochemical impedance spectroscopy (EIS) of  $\alpha\text{-Fe}_2\text{O}_3$  thin films were studied under the light in  $0.1\text{ M}$   $\text{Na}_2\text{SO}_4$  solution at various potentials from  $1.0$  to  $1.6\text{ V}$  vs. RHE. The applied frequency ranged from  $10\text{ }\mu\text{Hz}$  to  $1\text{ MHz}$  with an amplitude of  $10\text{ mV}$ . The measured EIS data was fitted using the Zview software. The Mott–Schottky (M–S) studies were carried out in a three-electrode system in  $0.1\text{ M}$   $\text{Na}_2\text{SO}_4$  solution (in the dark). Frequencies of  $1$  and  $2\text{ kHz}$ ,  $10\text{ mV}$  amplitude, in the potential range from  $0$  to  $1.0\text{ V}$  vs. RHE were applied.

### 2.4. PEC degradation of B41 dye

The degradation of B41 was conducted in a two-compartment PEC cell comprising photoanodic ( $75\text{ mL}$ ) and cathodic ( $55\text{ mL}$ ) chambers separated by a proton exchange membrane (Nafion-115) (Fig. S1). All the experiments were performed at  $25^\circ\text{C}$  using  $\alpha\text{-Fe}_2\text{O}_3$  thin film as a working electrode (area  $6\text{ cm}^2$ ),  $\text{Hg}/\text{Hg}_2\text{SO}_4$  electrode as the reference electrode, and a graphite plate as the counter electrode. The counter and working electrodes are kept  $3\text{ cm}$  apart. The dye degradation was studied in the presence of different supporting electrolytes such as NaCl,  $\text{NH}_4\text{Cl}$ , and  $\text{Na}_2\text{SO}_4$ . An LED light source ( $\lambda_{\text{ex}} 400\text{ nm}$ ,  $20\text{ W}$ ) was used to illuminate the PEC system (distance  $\sim 7\text{ cm}$ ). The incident light intensity

(6 mW cm<sup>-2</sup>) was measured using an optical power meter (Thorlabs PM320E Dual-Channel Optical Power & Energy Meter Console). The LED light spectrum is provided in Fig. S1e. The degradation of B41 dye at different reaction times was monitored using a Perkin Elmer Lambda 25 UV-VIS spectrophotometer. The concentration of free chlorine species mainly as HOCl was estimated by measuring the absorbance at 515 nm of N,N-diethyl-p-phenylenediamine (DPD) colorimetric test kits (tube test Nanocolor chlorine/ozone 2, REF 985017) [7] with a UV-VIS spectrophotometer (Macherey Nagel, Nanocolor 500d) for a concentration range of 0.0–2.5 mg·L<sup>-1</sup>. Chemical oxygen demand (COD) of B41 solutions were determined using a colorimetric approach with K<sub>2</sub>Cr<sub>2</sub>O<sub>7</sub> (Macherey Nagel, Nanocolor CSB 160). The HPLC-UV-Vis (from now on just HPLC) analyses were carried out on an Agilent 1100 system using a Phenomenex C18 Luna column (dimensions 150 × 2.0 mm; particle size: 3 μm) at 50 °C. Injection volume of the samples was 5 μL. Gradient elution was performed using 5 mM H<sub>2</sub>SO<sub>4</sub> aqueous solution (mobile phase A) and acetonitrile (mobile phase B) from 0 min (100% A) to 17 min (30% A and 70% B) at the flow rate of 0.3 mL min<sup>-1</sup>. Three detection wavelengths were chosen: 210 and 600 nm. Cyclic voltammetry (CV) was used to measure (scan rate: 50 mV s<sup>-1</sup>) the redox potentials of B41 dye using glassy carbon as the working electrode, graphite as the counter electrode, and Ag/Ag<sup>+</sup> electrode as the pseudo-reference electrode. Formation of •OH radicals was studied using photoluminescence measurements (FL920 spectrophotometer, Edinburgh Instruments) with coumarin. GC-MS from Agilent (5977B GC/MSD) was employed for identifying mass spectra of degraded products (GC-MS conditions described in Supplementary Information).

### 3. Results and discussion

#### 3.1. Characterization of α-Fe<sub>2</sub>O<sub>3</sub> photoanode

XRD patterns of the pure FTO/glass substrate and the α-Fe<sub>2</sub>O<sub>3</sub> thin film deposited onto the FTO/glass are shown in Fig. 1. The intense diffraction peaks at 35.58° and 63.91° (2θ) correspond to (104) and (300) crystal planes of the hexagonal α-Fe<sub>2</sub>O<sub>3</sub> (R3c (167); PDF# 2101169). The crystallite sizes of α-Fe<sub>2</sub>O<sub>3</sub> calculated using the Scherrer's gave an average size of 38 nm. Besides α-Fe<sub>2</sub>O<sub>3</sub> peaks, intensive peaks are seen from the FTO substrate. These intense diffraction peaks were indexed to the SnO<sub>2</sub> phase typical for tetragonal rutile structure (P42/mnm; PDF# 2101853).

UV-VIS spectroscopy was used to determine the optical band-gap ( $E_g$ ) of α-Fe<sub>2</sub>O<sub>3</sub> film (Fig. 2). Using the Tauc equation and assuming an indirect transition, the  $E_g$  is estimated from the following relation:  $(\alpha h\nu)^{1/n} = A(h\nu - E_g)$ , where  $\alpha$  is the linear absorption coefficient of the material,  $h\nu$  is photon energy, and  $A$  is a proportionality constant. The  $E_g$  value taken from the intercept is equal to ~2.0 eV (inset in Fig. 2). This

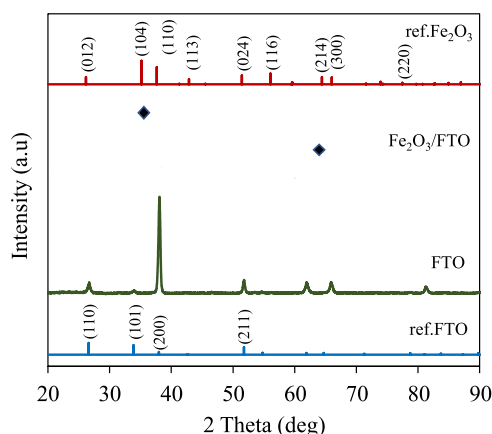


Fig. 1. XRD patterns of FTO (F:SnO<sub>2</sub>) and α-Fe<sub>2</sub>O<sub>3</sub> coated on FTO substrates.

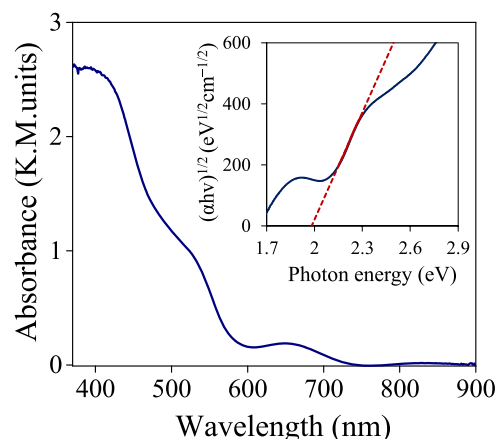


Fig. 2. An absorbance spectrum of α-Fe<sub>2</sub>O<sub>3</sub> thin film. The inset is a Tauc plot.

value matches the  $E_g$  of α-Fe<sub>2</sub>O<sub>3</sub> reported in the literature (1.9 – 2.2 eV) [46,47].

Structural characterization of α-Fe<sub>2</sub>O<sub>3</sub> was achieved using TEM. A scratch made on the α-Fe<sub>2</sub>O<sub>3</sub> film allowed us to collect materials on the Cu grid. Fig. 3a shows an agglomerate composed of Fe<sub>2</sub>O<sub>3</sub> particles. High-resolution TEM showed that the lattice spacing is equal to 0.185 nm, which closely matches with the (024) crystal plane of hexagonal α-Fe<sub>2</sub>O<sub>3</sub> (Fig. 3b). The selected area electron diffraction (SAED) pattern shows that these particles are polycrystalline (Fig. 3c) [48]. The diffraction rings in the SAED pattern can be indexed to the (104), (110), (116), and (214) of α-Fe<sub>2</sub>O<sub>3</sub>. Elemental mapping was used to determine the ratio and distribution of elements in the α-Fe<sub>2</sub>O<sub>3</sub>. Fig. 3e, f shows uniform distribution of Fe and O elements (at% ratio 2:3) in the agglomerate. The morphology of the α-Fe<sub>2</sub>O<sub>3</sub> film was studied using SEM. Thermal annealing in air at 750 °C generates a porous α-Fe<sub>2</sub>O<sub>3</sub> film (Fig. 3g, h). The pore (e.g., void) formation was ascribed to the PVP polymer, which after heat treatment at 450 °C burns and generates these voids. In earlier studies, it was shown that adding organic polymers such as PVP as a pore-forming agent allows fabricating porous metal oxide thin films and achieve an improvement in the photocurrent performance [49,50]. To estimate the film thickness and achieve better image contrast between different phases, a SEM image was acquired using a back-scattered electron detector. Fig. 3h shows a cross-section view of the electrode where the FTO layer appears slightly brighter, while the α-Fe<sub>2</sub>O<sub>3</sub> layer is a little darker. The film thickness was found to be about 303 nm. The voids seen inside the α-Fe<sub>2</sub>O<sub>3</sub> film are because of overlapping α-Fe<sub>2</sub>O<sub>3</sub> layers formed during two subsequent coating and heating processes. Further, EDX lines of Fe and O elements were used to confirm the stoichiometric composition of α-Fe<sub>2</sub>O<sub>3</sub> (Fig. 3i).

Fig. 4a shows the linear sweep voltammogram (LSV) of α-Fe<sub>2</sub>O<sub>3</sub> thin film in the dark and under illumination ( $\lambda_{\text{ex}}$ , 400 nm) in 0.1 M Na<sub>2</sub>SO<sub>4</sub>. The lack of photocurrent under dark in the potential range from 0.6 to 1.6 V vs. RHE shows that the film is not catalytically active. However, upon illumination, the steep increase of current density above 0.88 V vs. RHE (the onset potential) shows that water oxidation reactions (O<sub>2</sub> evolution) occur at the electrode surface. Further, the stability of the Fe<sub>2</sub>O<sub>3</sub> thin film was studied by recording the photocurrent at an applied bias of 1.5 V versus the RHE (see inset in Fig. 4a). The results confirmed that the α-Fe<sub>2</sub>O<sub>3</sub> photoanode shows decent stability during the 4 h test. The drop of photocurrent stabilized at 1.5 mA starting from the initial value of 2.0 mA. The effective electrochemical active surface area (ECSA) determined from the double-layer capacitance ( $C_{dl}$ ) of the electrode surface was obtained from EIS data in a non-Faradic region. Fig S2 shows a Nyquist plot for α-Fe<sub>2</sub>O<sub>3</sub> thin film in the frequency range from 0.1 Hz to 10 kHz recorded with an amplitude of 10 mV. The calculated ECSA is found to be around 1.96 cm<sup>2</sup> which is much higher than the geometrical area (~0.283 cm<sup>2</sup>) (Table S1). In the present work, the



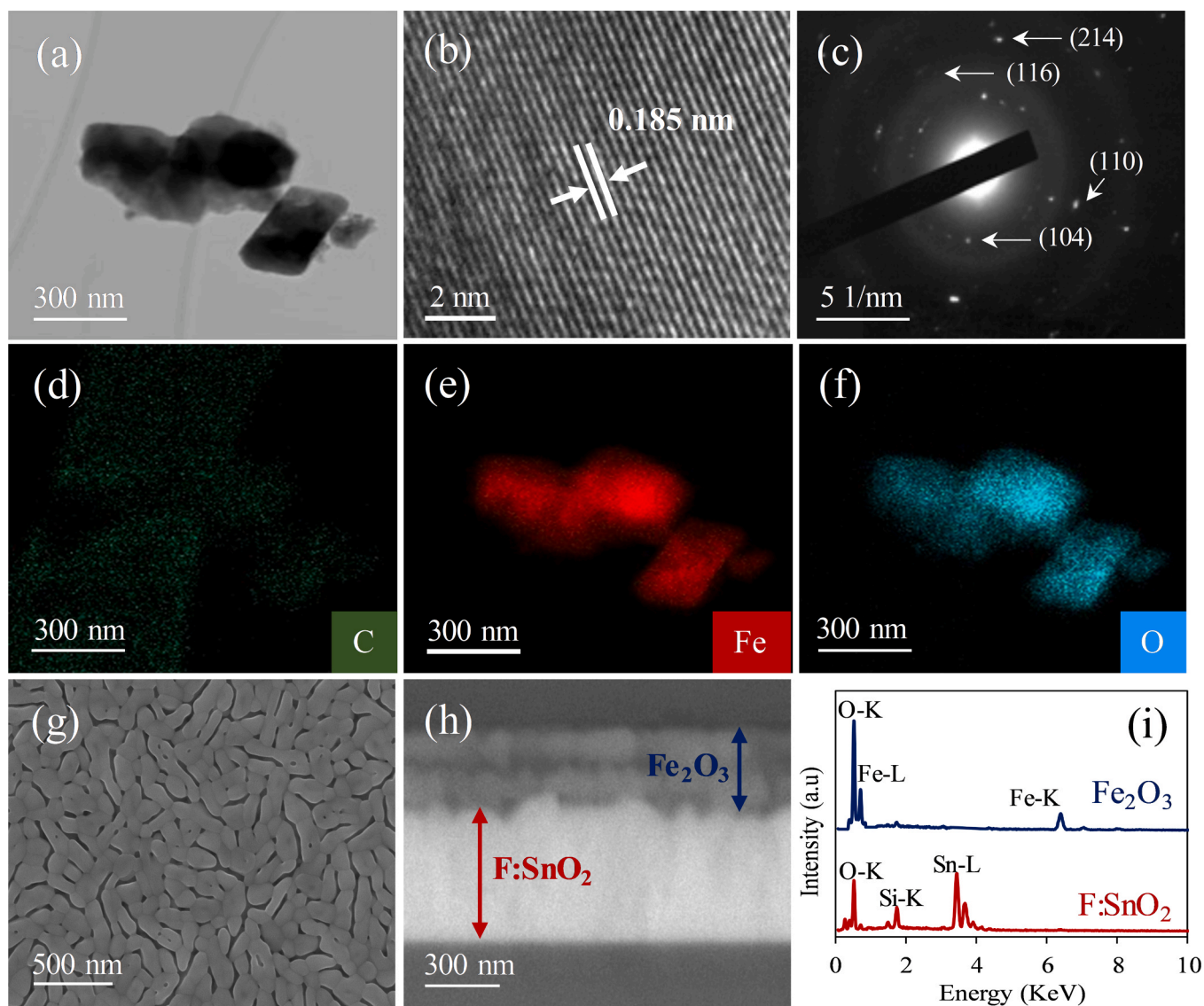


**Fig. 3.** (a) Bright-field STEM image of  $\alpha$ -Fe<sub>2</sub>O<sub>3</sub> and its corresponding element maps of (d) C, (e) Fe and (f) O. (b) HR-TEM image of  $\alpha$ -Fe<sub>2</sub>O<sub>3</sub> lattice and (c) SAED pattern taken from (a). Top-view (g) and cross-section view (h) of the  $\alpha$ -Fe<sub>2</sub>O<sub>3</sub> thin film. In (i) are given the EDX spectra recorded from the image in (h) for the FTO and  $\alpha$ -Fe<sub>2</sub>O<sub>3</sub> layers.

photocurrent density of film ( $\text{mA cm}^{-2}$ ) was given based on its geometric area unless specified to its ECSA. With the goal to construct the energy diagram of  $\alpha$ -Fe<sub>2</sub>O<sub>3</sub>, M–S studies were conducted at several frequencies. Fig. 4b shows an M–S plot of  $\alpha$ -Fe<sub>2</sub>O<sub>3</sub> film where the curves exhibit a positive slope, which is an indicator for an *n*-type semiconductor. An important parameter of the semiconductor electrodes is its flat-band potential ( $V_{\text{FB}}$ ). According to the depletion layer model, the capacitance of the semiconductor space charge layer (C) depends on the applied potential (V) and can be estimated from the M–S equation [25]:

$$\frac{1}{C^2} = \left( \frac{2}{e\epsilon_0\epsilon A^2 N_D} \right) \left[ (V - V_{\text{FB}}) - \frac{KT}{e} \right] \quad (1)$$

Where  $e$  is the electron charge,  $\epsilon_0$  is the vacuum permittivity,  $\epsilon$  is the dielectric constant of  $\alpha$ -Fe<sub>2</sub>O<sub>3</sub> ( $\epsilon = 80$ ) [51,52],  $A$  is the surface area of the electrode,  $k$  is the Boltzmann constant,  $N_D$  is the donor density, and  $T$  is the absolute temperature. Extrapolating the linear region of the M–S curve and reading the intercept value on the abscissa gives the  $V_{\text{FB}}$ . The obtained  $V_{\text{FB}}$  values are equal to 0.28 V at 1 kHz, and 0.25 V at 2 kHz vs. RHE, which are close to the literature reported values [51]. The  $N_D$  values were determined from the slope (S) in the M–S plot by the

following formula [53]:

$$N_D = \frac{2}{e\epsilon_0\epsilon A^2 S} \quad (2)$$

The calculated  $N_D$  values of the  $\alpha$ -Fe<sub>2</sub>O<sub>3</sub> film are equal to  $2.14 \times 10^{20}$  (1 kHz), and  $1.40 \times 10^{20} \text{ cm}^{-3}$  (2 kHz), which are comparable with the reported value  $6.1 \times 10^{20} \text{ cm}^{-3}$  for  $\alpha$ -Fe<sub>2</sub>O<sub>3</sub> thin films [25,54]. To understand the origin of the PEC activity, EIS studies were performed using the  $\alpha$ -Fe<sub>2</sub>O<sub>3</sub> thin film. Fig. 4c shows the Nyquist plot under different applied potentials in the range from 1.0 to 1.6 V vs. RHE. As expected, with the increase of bias potential, the recorded impedance signal decreases. After fitting the EIS data with an appropriate equivalent circuit, the charge transfer resistance was obtained (Fig. 4d). The circuit element consists of a series resistance ( $R_s$ ), the charge-transport resistance in bulk ( $R_1$ ) given with the semi-circles observed in the high frequency region, and the constant phase element (Q1) which relates to the capacitance of bulk material. The higher arc in the low frequency region reflects the charge transfer resistance at the electrode/electrolyte interface ( $R_2$ ) and the space charge layer capacitance (Q2) [55,56]. The  $R_2$  represents the hole-to-oxygen transfer resistance during water

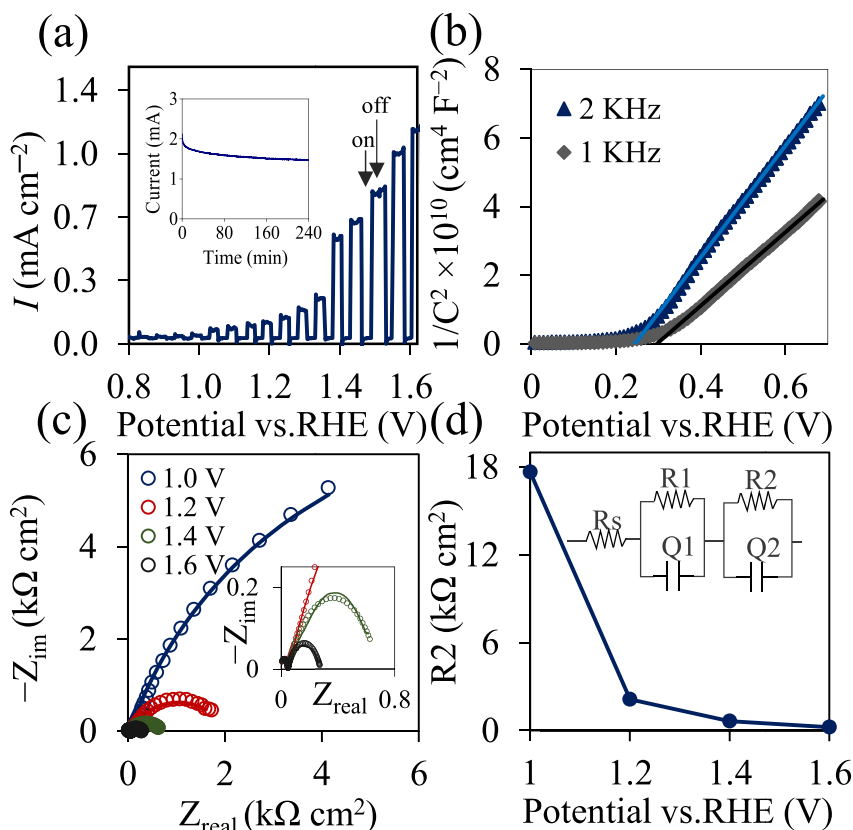


**Fig. 4.** (a) LSV of  $\alpha$ -Fe<sub>2</sub>O<sub>3</sub> in 0.1 M Na<sub>2</sub>SO<sub>4</sub> (pH 5) under chopped illumination. The inset is a current vs. time recorded at 1.5 V vs. RHE. (b) M-S plot of  $\alpha$ -Fe<sub>2</sub>O<sub>3</sub> photoanode in 0.1 M Na<sub>2</sub>SO<sub>4</sub>. (c) Nyquist plot of  $\alpha$ -Fe<sub>2</sub>O<sub>3</sub> thin film in 0.1 M Na<sub>2</sub>SO<sub>4</sub> under illumination. (d) Charge transfer resistance ( $R_2$ ) versus applied voltages (inset is the equivalent circuit element).

oxidation reaction. EIS measurement of  $\alpha$ -Fe<sub>2</sub>O<sub>3</sub> showed low  $R_2$  at higher bias voltages, which indicates a fast charge-transfer kinetics.

### 3.2. PEC degradation of B41 dye

The textile B41 dye was used as a model pollutant in PEC degradation studies (Table S2). Fig. 5a shows the absorption spectra of B41 dye in 0.02 M NaCl at various degradation time intervals using PEC. The degradation of B41 using  $\alpha$ -Fe<sub>2</sub>O<sub>3</sub> thin film was monitored by taking aliquots and recording the absorption peak at 610 nm. The degradation efficiency ( $D$ ) was calculated using the following equation:  $D(\%) = (C_0 - C)/C_0 \times 100$  (Fig. S3), where  $C_0$  is the concentration at zero time ( $t = 0$  min) and  $C$  is the concentration at the specified reaction time [21]. Fig. 5b displays the degradation of B41 using different approaches in 0.02 M NaCl. In the case of EC approach B41 degradation was limited to 22.1%. Similarly, the photocatalysis (PC) approach also yielded low degradation values in the order of 12.6%. In the presence of Cl<sup>-</sup> using the PEC approach the degradation increased significantly (99.8%), thus indicating that RCS promote the dye decomposition. COD approach was used to prove the mineralization of B41 dye. For the PEC experiment in 0.02 M NaCl the COD levels dropped from 149 mg L<sup>-1</sup> (before treatment) to 49 mg L<sup>-1</sup> after 70 min. Therefore, the PEC treatment allows partial mineralization of B41 dye.

A pseudo-first-order kinetic was used to fit the experimental data using the following equation:  $\ln(C/C_0) = -k_1 t$ , where  $C$  and  $C_0$  are the concentrations of dye at time  $t$  and time zero, and  $k_1$  is the first order rate constant (see Table S3). Using the PEC approach, in the presence of Cl<sup>-</sup> ions,  $k_1 = 0.0881 \text{ min}^{-1}$  was found to be 23 and 41 times higher than EC ( $k_1 = 0.0038 \text{ min}^{-1}$ ) and PC ( $k_1 = 0.0021 \text{ min}^{-1}$ ), respectively (Fig. 5c). The obtained  $k_1$  constants in Cl<sup>-</sup> electrolyte using  $\alpha$ -Fe<sub>2</sub>O<sub>3</sub> in this work are higher than other photoanodes reported in earliest studies. For

example, using CdS/TiO<sub>2</sub> catalyst during MB degradation under PEC condition yielded  $k_1 = 0.0109 \text{ min}^{-1}$  [57].

The PEC degradation of B41 in 20 mM NaCl is associated with different species such as  $\bullet$ OH and RCS [58]. In agreement with this hypothesis, the evolution of RCS (e.g., HOCl/OCl<sup>-</sup>) was measured in the PEC system using the DPD colorimetric method [7]. The generated HOCl is over 2.5 mg L<sup>-1</sup> in 15 min (pH 5) (Fig. S4). This measurement shows that HOCl is formed and its concentration gradually increased during the dye degradation process. The results are consistent with the PEC-chlorine system where HOCl plays an essential role during degradation of acetaminophen, bisphenol A, and carbamazepine degradation in acid condition using WO<sub>3</sub> photoelectrodes [7]. In a similar way, Zaroni et al. also showed that oxidation of Cl<sup>-</sup> to HOCl at TiO<sub>2</sub> photoanode occurs and the RCS generation has been proposed to help the PEC degradation of organic compounds [6,10,59,60]. Another indicator used to prove the generation of RCS during PEC was to monitor the formation of Cl<sub>2</sub> using mass spectrometry (MS). From the photoanode compartment a Cl<sub>2</sub> gas was collected using a syringe and later injected it into the MS capillary tube. Fig. 5d shows MS data which confirm the presence of Cl ( $m/z = 35$ ); Cl<sub>2</sub> ( $m/z = 70$ ) and CO<sub>2</sub> ( $m/z = 44$ ) species. The formation of CO<sub>2</sub> was ascribed to the mineralization of B41 dye during the degradation process.

### 3.3. Dye degradation experiments under different conditions

To understand the mechanism of dye degradation, different molecules/species were used as scavengers for photogenerated holes (EDTA),  $\bullet$ OH radicals (TBA), and RCS (Na<sub>2</sub>S<sub>2</sub>O<sub>3</sub>) (Fig. 6a). It is interesting to note that PEC degradations of organic compounds could involve reactive oxygen species (ROS) such as  $\bullet$ OH radicals. The photogenerated holes in the valence band of  $\alpha$ -Fe<sub>2</sub>O<sub>3</sub> could react with water molecules (H<sub>2</sub>O) and

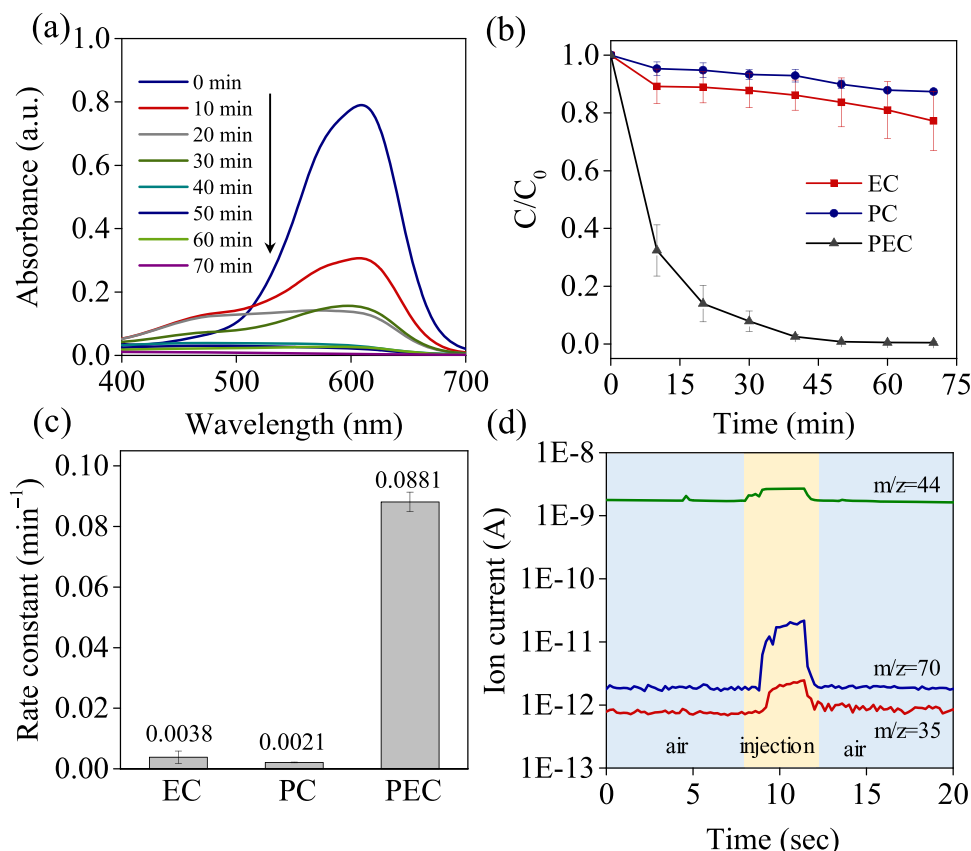
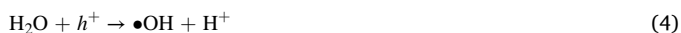


**Fig. 5.** (a) Absorption spectra of B41 dye recorded during PEC experiment. (b) Normalized concentration ( $C/C_0$ ) of B41 dye vs. time for EC, PC and PEC recorded in 0.02 M NaCl. (c) Average reaction rate constant ( $\text{min}^{-1}$ ) for degradation of B41. (d) Ionic current vs. time of Cl,  $\text{Cl}_2$ , and  $\text{CO}_2$  recorded using MS.

generate  $\bullet\text{OH}$  radicals, while the photogenerated electrons in the conduction band converted the molecular oxygen into superoxide radical anion ( $\text{O}_2^{\bullet-}$ ) which on protonation yields  $\text{HO}_2^{\bullet}$  radicals and  $\text{H}_2\text{O}_2$  [23,24]. The generation of  $\bullet\text{OH}$  radicals may also involve a reaction between  $\text{H}_2\text{O}_2$  and  $\text{O}_2^{\bullet-}$ . These possible reactions are given with Eqs. (3)–(8).



It is well known that EDTA is a good scavenger for the photo-generated holes [7]. In the present system EDTA indirectly blocks the formation of RCS (see Eq. (12)) and ROS species which result in lower dye degradation efficiency. On the other hand, TBA is an efficient scavenger of  $\bullet\text{OH}$  radicals yielding a rate constant of  $5 \times 10^8 \text{ M}^{-1} \text{ s}^{-1}$  [61]. In the present system when TBA was used as a scavenger, the degradation of B41 dye is quite efficient which implies that generation of  $\bullet\text{OH}$  radicals is negligible [11]. To probe the formation of  $\bullet\text{OH}$  radicals coumarin was also used as a qualitative probe. It is well known that coumarin reacts with  $\bullet\text{OH}$  radicals to form highly fluorescent 7-HC (peak at  $\sim 455 \text{ nm}$ ) [7,11]. The lack of emission peak from 7-HC in  $\text{Cl}^-$  containing electrolyte suggest that  $\bullet\text{OH}$  radicals' formation is suppressed (Fig. S5). Adding in the solution  $\text{Na}_2\text{S}_2\text{O}_3$  scavenger inhibits the generation of RCS (e.g.,  $\text{HOCl}$ ), which in turns give lower dye degradation efficiency. Therefore, RCS plays a major role in the degradation of B41 dye. A comparative study between PEC and chemical oxidation

with  $\text{NaOCl}$  (form of RCS) was also given in this study (Fig. 6b). Different concentrations of  $\text{NaOCl}$  electrolyte were added in the dye solution to drive the B41 dye decolorization. It was found that approximately 6 mM  $\text{NaOCl}$  was sufficient for dye decolorization which is comparable to PEC approach. This indicates that the decolorization of B41 is driven by in-situ generated RCS species.

As stated in earlier studies on PEC decomposition of azo dyes, applied anodic potential can significantly affect the efficiency of dye degradation [59]. The effect of anodic potentials on B41 dye degradation were studied at different bias voltages (Fig. S6). As expected, the results indicate that the degradation efficiency increased with the applied bias potential. As the anodic potential varied from 1.0 to 1.5 V vs. RHE, the photocurrent vs time ( $I-t$ ) increased from 0.05 to  $0.3 \text{ mA cm}^{-2}$ . This explained that the photoelectric conversion efficiency could be improved at higher applied anodic potential, as it also makes an external electric field that suppress the recombination of the photogenerated electron-hole pairs [62].

A comparison of PEC degradation was given in different electrolytes:  $\text{NaCl}$ ,  $\text{NH}_4\text{Cl}$  and  $\text{Na}_2\text{SO}_4$ . The LSV characteristics of  $\alpha\text{-Fe}_2\text{O}_3$  film recorded in these electrolytes together with the Tafel plot are provided in Fig. S7. As expected, the fastest degradation occurs in the presence of  $\text{NaCl}$  electrolyte (Fig. 7a). It seems that chloride ions rapidly react with the photogenerated holes, retarding the recombination of charge pairs, giving rise to higher photocurrent (Fig. S7a). The slower degradation in  $\text{NH}_4\text{Cl}$  electrolyte is due to competitive oxidation of ammonium cation ( $\text{NH}_4^+$ ) and B41 dye. The RCS generated in the PEC system includes  $\text{HOCl}/\text{OCl}^-$  and chlorine-based radicals (i.e.,  $\text{Cl}\bullet$ ,  $\text{Cl}_2\bullet^-$ ). The  $\text{Cl}\bullet$  produced by the photogenerated holes could oxidize the electron-rich  $\text{NH}_4^+$  ion to intermediate chloramine or  $\text{N}_2$  [63]. Ji et al., reported a selective transformation reaction of ammonia nitrogen to  $\text{N}_2$  with  $\text{Cl}\bullet$  using  $\text{WO}_3$  photoanode [64]. Similarly, Zhang et al., demonstrated efficient

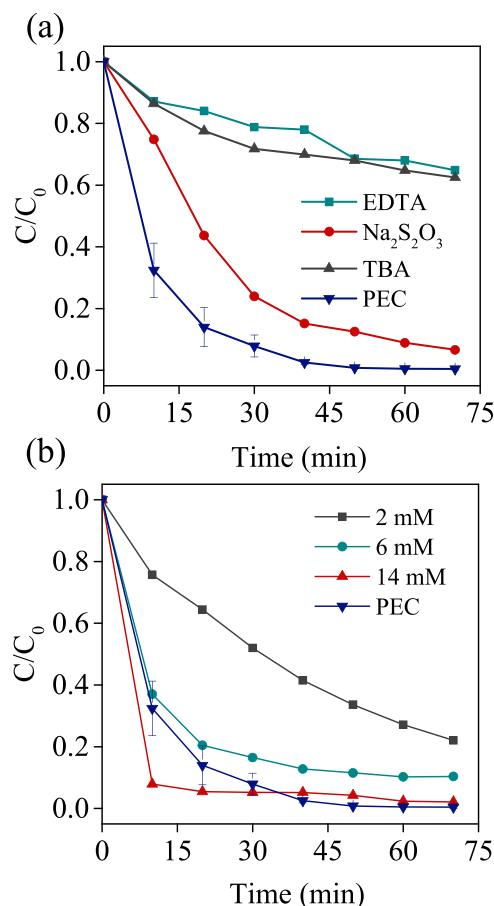


**Fig. 6.** (a) Normalized concentration of B41 dye during PEC degradation in the presence of 20 mM NaCl and different scavengers: 0.1 M TBA, 0.1 M EDTA, and 0.1 M  $\text{Na}_2\text{S}_2\text{O}_3$ , pH 5. (b) Comparison of B41 degradation using PEC and chemical oxidation at different NaOCl concentrations.

removal of ammonia using  $\text{BiVO}_4/\text{WO}_3$  photoanode [65]. On the other side, in  $\text{NH}_4^+$  free systems the kinetic rate constant,  $k(\text{Cl}\bullet)$ , between  $\text{Cl}\bullet$  and most aromatic molecules varies between  $10^8 - 10^{10} \text{ M}^{-1} \text{ s}^{-1}$  [66, 67]. These high values allow efficient degradation of organics. When  $\text{Na}_2\text{SO}_4$  electrolyte was used, slow degradation of B41 was observed. In  $\text{Cl}^-$  free environment only 48.9% of B41 was degraded after 70 min reaction. Here the degradation was attributed to the  $\text{SO}_4^{\bullet-}$  and  $\bullet\text{OH}$  oxidizing species. However, in acidic environment  $\text{SO}_4^{\bullet-}$  radicals are less effective than  $\bullet\text{OH}$  radicals which form favorably in alkaline solutions [68]. At pH 5 the generation of  $\bullet\text{OH}$  is favored to occur unfavorably. A simple comparison of  $\alpha\text{-Fe}_2\text{O}_3$  film used in this study with the literature reports showed that degradation is faster in the presence of  $\text{Cl}^-$  ion (Table S4). Fig. 7b shows the effect of NaCl concentration on the degradation efficiency of B41 with  $\alpha\text{-Fe}_2\text{O}_3$  photoanode. The fastest dye degradation is observed when the concentration of NaCl was set to 200 mM. However, the use of high concentration of NaCl is needless and in further PEC studies this value was fixed to 20 mM. The effect of pH on PEC degradation of B41 was investigated at pH 5 and 7 (Fig. 7c). The degradation process was faster at pH 5. The enhanced reactivity at low pH may be explained by the dominant presence of chlorine radicals (e.g.,  $\text{Cl}\bullet$ ,  $\text{Cl}_2\bullet^-$ ) or active chlorine species ( $\text{HOCl}$ ) over  $\bullet\text{OH}$  [10]. Another reason for the slower reaction at pH 7 is that the  $V_{\text{FB}}$  edge potential of  $\alpha\text{-Fe}_2\text{O}_3$  moves to the negative direction, reducing the driving force of  $\text{Cl}^-$  ion oxidation [7].

Series of PEC experiments were also conducted at different initial concentrations of B41 dye ranging from 20 to 50  $\mu\text{M}$  (Fig. 7d). As expected, dye degradation is slow when the initial concentration of B41 dye is high, which obey with the trend observed during the PEC

degradation of other organics pollutant [69]. The kinetic reaction that describes the azo dye photooxidation process can be associated with the Langmuir–Hinshelwood (L–H) model [70]:

$$r_0 = \frac{k_r K C_0}{1 + K C_0} \quad (9)$$

where  $r_0$  is the initial rate of reaction ( $\text{M min}^{-1}$ ),  $k_r$  is the L–H reaction rate constant ( $\text{M min}^{-1}$ ),  $K$  is the L–H adsorption equilibrium constant ( $\text{M}^{-1}$ ) and  $C_0$  is the initial concentration of dye ( $\text{M}$ ). The Langmuir–Hinshelwood mechanism assumes surface chemical reaction between adsorbed species. The adsorbed dye molecules on the electrode surface could participate in direct oxidation with the holes ( $h^+$ ) from the semiconductor. However, photoelectrocatalytic dye degradation involves parallel reactions with adsorbed  $\text{Cl}^-$  ions or  $\text{H}_2\text{O}/\text{OH}^-$ . PEC oxidation of the latter species can yield RCS or  $\bullet\text{OH}$  radicals which can participate in indirect dye degradation [69,71]. Rearranging Eq. 9 with give the following expression [72]:

$$\frac{1}{r_0} = \frac{1}{k_r K C_0} + \frac{1}{k_r} \quad (10)$$

A plot of  $1/r_0$  versus  $1/C_0$  for PEC degradation of B41 in 20 mM NaCl shown in Fig. S8. The values of initial degradation rate  $r_0$  were determined from slopes of the concentration versus time plots. The values of  $k_r$  and  $K$  are estimated as following:  $k_r = 3.01 \times 10^{-6} \text{ M min}^{-1}$  and  $K = 3.35 \times 10^4 \text{ M}^{-1}$ . The high value of the constant  $K$  assumes a strong interaction of B41 with the  $\alpha\text{-Fe}_2\text{O}_3$  surface. The  $K$  constant is also connected to the standard free energy of adsorption,  $\Delta G^0$ , with the following equation [72]:

$$\Delta G^0 = -RT \ln K \quad (11)$$

Where  $R$  represent the gas constant ( $8.314 \text{ J mol}^{-1} \text{ K}^{-1}$ ),  $T$  is the absolute temperature (298.15 K). The value of free energy  $\Delta G^0$  is  $-25.8 \text{ kJ mol}^{-1}$  which can be calculated. The negative value of  $\Delta G^0$  indicate a spontaneous adsorption process of B41 on the  $\alpha\text{-Fe}_2\text{O}_3$  surface. In general, values of  $\Delta G^0$  around  $-20 \text{ kJ mol}^{-1}$  or higher are consistent for the electrostatic interaction between the charged molecules and the electrode [72,73]. As for the adsorption  $K$  constant of  $\text{Cl}^-$  on surfaces there are limited studies. Ferro et al., reported the value of  $K(\text{Cl}^-) = \sim 0.4 \text{ M}^{-1}$  in 0.01 M  $\text{HClO}_4$  and 0.1–2 M NaCl using  $\text{RuO}_2$  film [74]. So, competitive adsorption of B41 dye and  $\text{Cl}^-$  is expected to occur on  $\alpha\text{-Fe}_2\text{O}_3$  surface in the present system.

The reusability tests of  $\alpha\text{-Fe}_2\text{O}_3$  photoanode were performed in the presence of B41 for five cycles (Fig. 8). The  $\alpha\text{-Fe}_2\text{O}_3$  film showed over 99% degradation efficiency of B41. These results show that the  $\alpha\text{-Fe}_2\text{O}_3$  thin film is stable against corrosion and could be reused in PEC studies. To strengthen this conclusion, morphology of the electrode surface was studied using SEM. As shown in Fig. 9a–d, the  $\alpha\text{-Fe}_2\text{O}_3$  electrode kept its morphology unchanged after the PEC process, which confirms once again the suitability of this material in PEC wastewater treatment.

#### 3.4. HPLC and GC-MS analyses

To prove the degradation efficiency and mineralization of B41 dye, HPLC was used to check the formation of any by-products during PEC degradation. The HPLC chromatogram taken from a reference B41 sample shows a well-defined peak at 14.0 min (0 min) elution time using fixed detection wavelengths at 210 and 600 nm. The disappearance of the absorption peak of B41 dye at 600 nm at 70 min elution time indicates breaking of the azo bond in the dye molecule (Fig. 10a). During the degradation of B41 are detected, 210 nm wavelength, smaller peaks at 1.7, 12.0, 13.5 and 14.5 min (Fig. 10b). This indicated the destruction of the dye and appearance of new compounds that are structurally different from the parent compound. HPLC studies tests were also conducted with  $\text{NH}_4\text{Cl}$  and  $\text{Na}_2\text{SO}_4$  electrolytes, whereas the expected decrease of B41 absorbance values at 600 nm were little (Fig. S9a, b).



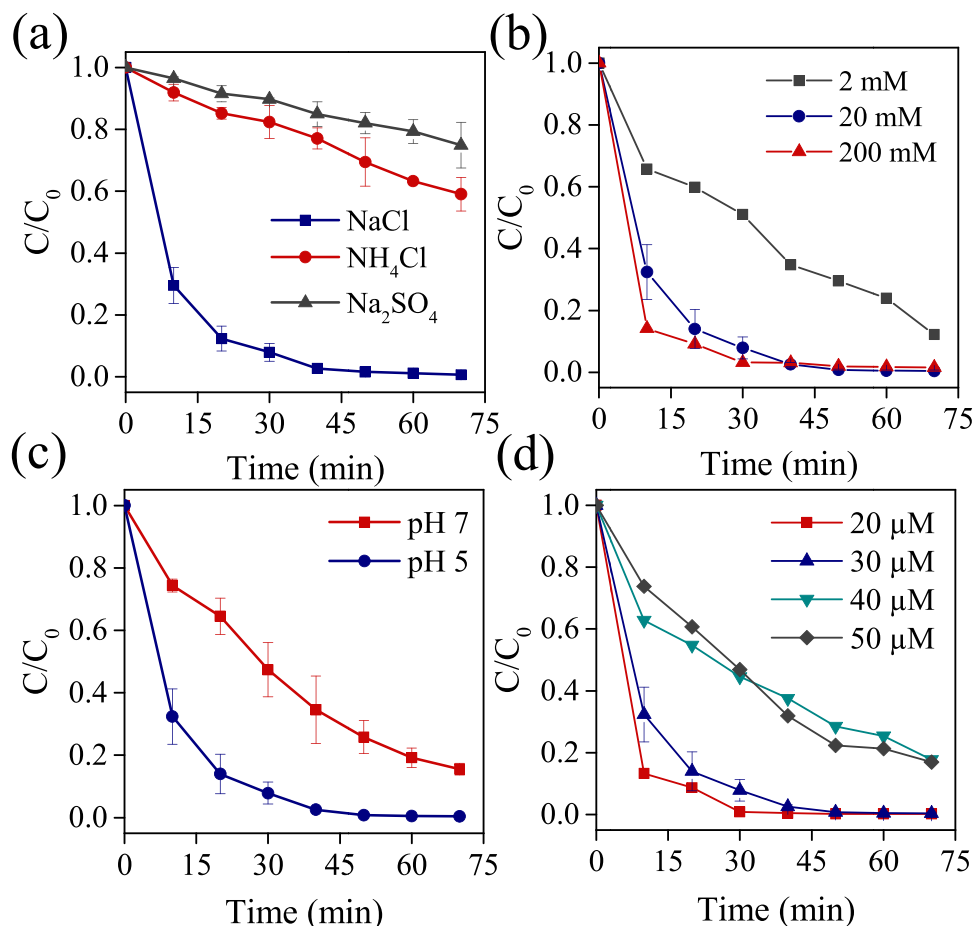


**Fig. 7.** Normalized dye concentration vs. time recorded using  $\alpha$ -Fe<sub>2</sub>O<sub>3</sub> thin films (PEC) at applied 1.5 V vs. RHE in: (a) different electrolytes (20 mM), (b) NaCl electrolyte (different concentrations), (c) different pH values and (d) varying dye concentrations in 20 mM NaCl.

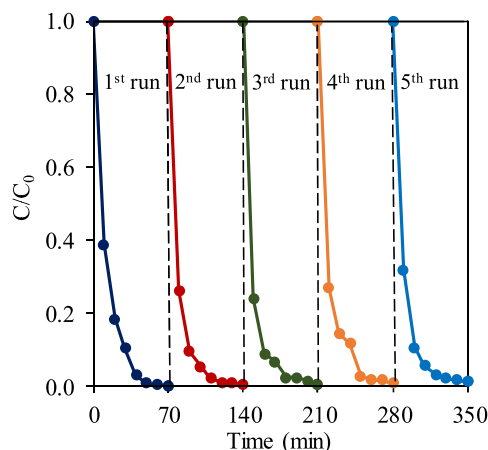


**Fig. 8.** PEC degradation of B41 dye for five runs at 1.5 V vs. RHE in 0.02 M NaCl.

Fig. 11 shows a plot of B41 concentration at different reaction times (detected at 600 nm). The concentration of B41 dye reduced from 12 mg L<sup>-1</sup> ( $t = 0$  min) to 0 mg L<sup>-1</sup> in 40 min. The results confirm that the  $\alpha$ -Fe<sub>2</sub>O<sub>3</sub> photoanode exhibits good catalytic activity for B41 degradation in NaCl electrolyte.

The degradation of B41 dye was also studied using GC-MS (Fig. S10). Aliquot was collected during the first 10 min of PEC degradation experiment. The total ion current chromatogram contains over 20 peaks

which belongs to different by-products. Some of the main intensive peaks are ascribed to 4-hydroxypentan-2-one ( $m/z$  102), 6-methyl-2,4-heptanedione ( $m/z$  142), ethanoic acid ( $m/z$  60), 3-amino-3-(4-hydroxyphenyl)-propanoic acid ( $m/z$  181), methylsulfanyl(methylsulfanyl) methane ( $m/z$  124), etc (Fig. S11). In the sample collected at 40 min PEC degradation time, the intensities of the chromatographic peaks were quite low and obstructed the identification of possible by-products.

### 3.5. Phytotoxicity test using *Lepidium sativum* L.

Seed germination and root growth of *L. sativum* was used to evaluate the phytotoxic effect of tested B41 dye solutions (Fig. S12). Inhibition (%), values are 6.7% and 8.5% for untreated and PEC treated B41 solutions, respectively (Fig. 12). The inhibition value for the untreated sample (before) is slightly lower in comparison after treatment, probably due to the formation of more toxic degradation by-products in PEC treated sample where root growth is inhibited. Worth mentioning that sometimes during EC or PEC degradation of organics in the presence of Cl<sup>-</sup> ions could also form toxic chlorinated molecules or chlorates [75]. Koo et al., studied the formation of toxic chlorate (ClO<sub>3</sub><sup>-</sup>) which is a secondary product from RCS reaction using WO<sub>3</sub> as photoanode in NaCl electrolyte. They showed that •OH radicals play a critical role in oxidizing Cl<sup>-</sup> to ClO<sub>3</sub><sup>-</sup> [7,75]. However, the formation of ClO<sub>3</sub><sup>-</sup> was recorded only under UV light but not under visible light irradiation [7]. It is assumed that in the present system the generation of ClO<sub>3</sub><sup>-</sup> is less likely to happen. Therefore, the observed slight toxicity in PEC treated water solution could be attributed to the different by-products as seen in GC-MS analyses. Other useful parameters evaluated for the untreated and PEC treated B41 solutions are the relative germination percentage



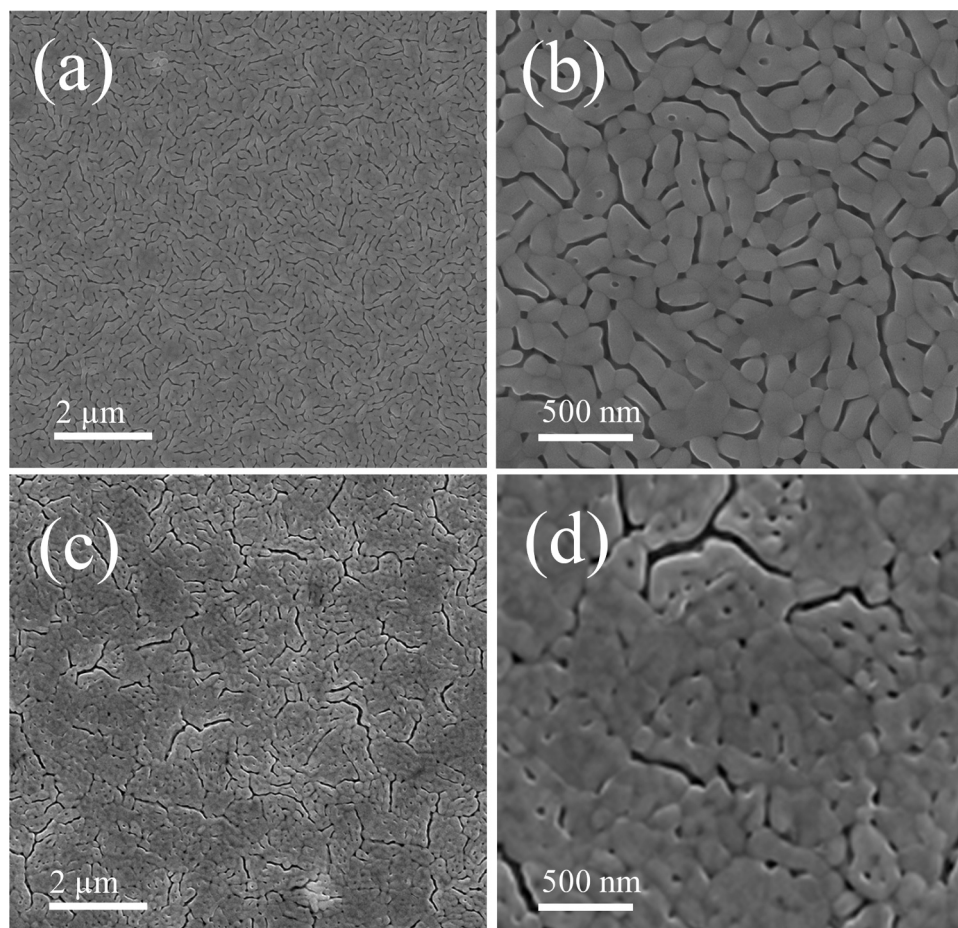


Fig. 9. SEM images of  $\alpha\text{-Fe}_2\text{O}_3$  thin film at different magnifications taken before (a, b) and after (b, c) the B41 dye degradation.

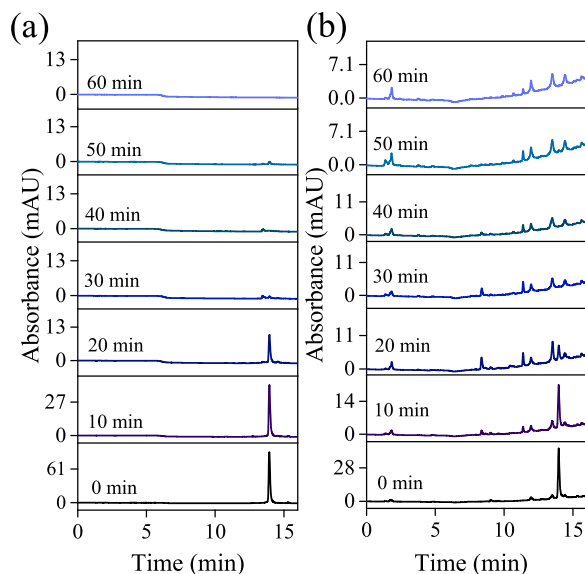


Fig. 10. HPLC chromatograms of B41 dye at different PEC degradation time in 0.02 M NaCl recorded at (a) 600 and (b) 210 nm detection wavelengths.

(%): 102.2 (before), 95.45 (after); relative radicle growth (%): 93.3 (before), 91.5 (after); and germination index (%): 95.46 (before), 87.3 (after). The treated water gives lower values for all parameters. The germination indexes in this study are above 80% which means that B41 solutions at the studied concentration ( $3 \times 10^{-5}$  M) level show low or

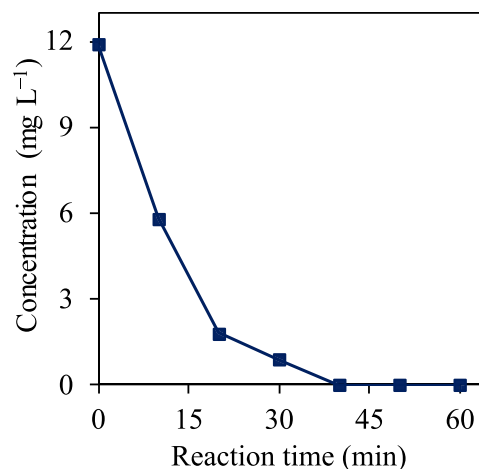


Fig. 11. Decrease of B41 concentration during PEC degradation in the presence of 0.02 M NaCl and bias potential of 1.5 V vs.RHE as determined using HPLC.

absence of phytotoxicity [76].

### 3.6. Degradation mechanism of B41 dye

The degradation process is primarily associated with the generation of photogenerated charges ( $e^-$  and  $h^+$ ) in  $\alpha\text{-Fe}_2\text{O}_3$  catalyst upon excitation with light. The photogenerated  $h^+$  at the photoanode has a strong capacity to oxidize water to  $\text{O}_2$  (1.23 V vs. RHE) [23,24]. In the presence

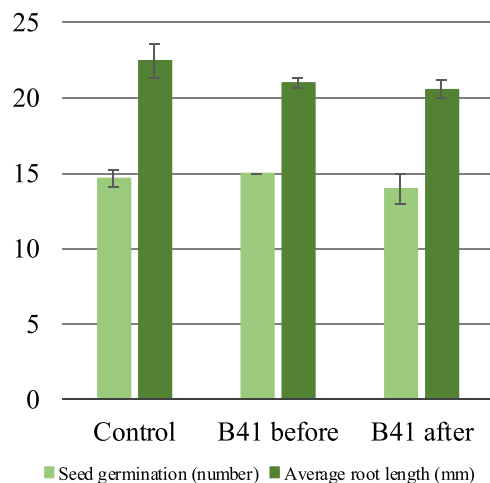


Fig. 12. Seed germination test for toxicity analysis of B41 solutions.

of  $\text{Cl}^-$  ions, water oxidation competes with the evolution of  $\text{Cl}_2$  ( $E^\circ = 1.36$  V) or sometimes the formation of the energy demanding  $\text{Cl}\bullet$  species ( $E^\circ = 2.47$  V vs. NHE) (see Eq. (12)–(15)) [1]. Further, the in-situ generated  $\text{Cl}_2$ , in an acidic medium (pH 5), will hydrolyze to  $\text{HOCl}$  as shown in Eq. (18).



It is unavoidable that in-situ generated  $\text{Cl}\bullet$  and  $\text{Cl}_2\bullet^-$  species along with the  $\text{HOCl}$  may take part in the oxidation of dye molecule. The experiments with TBA and coumarin showed that the  $\bullet\text{OH}$  radicals' generation is blocked (Eq. 4) [77]. Therefore,  $\bullet\text{OH}$  radicals do not participate in dye degradation in the presence of  $\text{Cl}^-$  electrolyte. In parallel to indirect oxidation, it could also happen a direct oxidation of B41 dye at the  $\alpha\text{-Fe}_2\text{O}_3$  surface. To prove this hypothesis, CV technique was used to measure the redox potentials of the B41 dye (Fig. 13a). Later, the highest occupied molecular orbital (HOMO) and lowest unoccupied molecular orbital (LUMO) energy levels of B41 dye is calculated. The HOMO level is determined from the first onset oxidation potential ( $E_{\text{ox}}$ ) at 0.88 V vs.  $\text{Ag}^+$ ,  $-E_{\text{HOMO}}(\text{eV}) = E_{\text{ox}} - E_{\text{Fc}} + 4.8$ , in which  $E_{\text{Fc}}$  is the oxidation potential of an internal reference molecule ferrocene ( $E_{\text{Fc}} = 0.15$  V) (Fig. 13a), assuming the reference energy level of ferrocene/ferrocenium is 4.8 eV below vacuum [78,79]. Therefore, the HOMO level of B41 dye is  $E_{\text{HOMO}} = -5.53$  eV. The LUMO level of B41 ( $E_{\text{LUMO}} = -3.49$  eV) is calculated from the following relation:  $E_{\text{LUMO}} = E_{\text{HOMO}} + (hc/\lambda)$ , where  $h$ ,  $c$  and  $\lambda$  are the Planck constant, the speed of light in vacuum and the maximum absorption light wavelength of B41 (610 nm), respectively. The energy diagram of  $\alpha\text{-Fe}_2\text{O}_3$  is constructed using the measured  $V_{\text{FB}}$  value (Fig. 13b). It has been reported that the conduction band (CB) potential ( $E_{\text{CB}}$ ) of  $n$ -type semiconductors is 0.1–0.2 V more negative than their  $V_{\text{FB}}$  values [25]. The CB of  $\alpha\text{-Fe}_2\text{O}_3$  is estimated as  $E_{\text{CB}} = 0.18$  V vs. RHE considering that  $V_{\text{FB}} = 0.28$  V vs. RHE at 1 kHz, assuming that the CB edge is 0.1 V more negative than  $V_{\text{FB}}$  (Fig. 4b). With an  $E_g$  value of  $\sim 2.0$  eV for  $\alpha\text{-Fe}_2\text{O}_3$ , the estimated valence band edge ( $E_{\text{VB}}$ ) comes out to be 2.18 V vs. RHE. The results show that the  $E_{\text{CB}}$  of  $\alpha\text{-Fe}_2\text{O}_3$  is located lower than the HOMO of B41, which shows a good alignment to sustain direct oxidation of B41 dye. The PEC

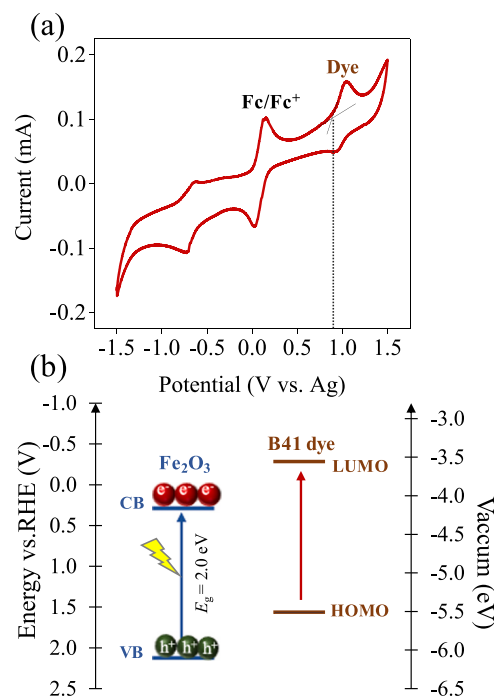


Fig. 13. (a) CV of 1 mM B41 dye in acetonitrile recorded at a scan rate of  $50 \text{ mV s}^{-1}$  in 0.1 M tetrabutylammonium perchlorate and 1 mM ferrocene (internal reference). (b) The energy diagram of  $\alpha\text{-Fe}_2\text{O}_3$  and B41 dye is shown.

experiments in  $\text{Na}_2\text{SO}_4$  electrolyte proved that direct oxidation of B41 dye is less likely to happen since this reaction proceed slowly. It can be concluded that the faster oxidation in the presence of  $\text{Cl}^-$  is because of the in-situ generated RCS species.

#### 4. Conclusions

An elegant method is presented for preparing porous  $\alpha\text{-Fe}_2\text{O}_3$  thin films based on spin-coating and subsequent heat-treatment at elevated temperatures. The procedure allows precise control over  $\alpha\text{-Fe}_2\text{O}_3$  film thickness ( $\sim 300$  nm). Detailed electrochemical analyses of the  $\alpha\text{-Fe}_2\text{O}_3$  electrode were performed using techniques like flat-band measurements, EIS, and LSV. The prepared  $\alpha\text{-Fe}_2\text{O}_3$  is a promising dual-function catalyst for water oxidation and dye degradation. For the first time, the  $\alpha\text{-Fe}_2\text{O}_3$  thin films were used in PEC degradation of B41 dye in the presence of  $\text{Cl}^-$  and  $\text{SO}_4^{2-}$  ions. To find the optimum conditions for B41 dye degradation, various parameters were studied such as dye loading, bias potential, pH, or different electrolytes. Results show that  $\text{NaCl}$  electrolyte gave the fastest dye degradation at pH 5. HPLC and GC-MS studied were used to monitor the degradation of B41 dye and the evolution of by-products. COD tests confirm that in  $\text{Cl}^-$  electrolyte the mineralization efficiency is about 68% after the PEC treatment (70 min). A comparison of B41 dye degradation was also conducted using EC, PC and PEC approaches. While the EC and PC give poor degradation efficiency, the PEC system yields 99.8% efficiency. The  $\alpha\text{-Fe}_2\text{O}_3$  thin films yields efficient degradation of B41 dye because of in-situ RCS formed in the PEC system.

#### CRedit authorship contribution statement

**M. Machreki:** conducted the experiments, analyzed the data, and wrote the manuscript. **T. Chouki:** contributed to DPD and COD measurements. **M. Martelanc:** carried out the HPLC and GC-MS measurements. **L. Butinar** contributed to phytotoxicity tests, fund raising and manuscript editing. **B.M. Vodopivec:** contributed to fund raising and manuscript editing. **S. Emin:** supervised the work, contributed to data

analysis, manuscript writing and editing, fund raising and Project Administration.

## Declaration of Competing Interest

The authors declare that they have no known competing financial interests or personal relationships that could have appeared to influence the work reported in this paper.

## Acknowledgements

This work was supported by the Slovenian Research Agency (ARRS) under the bilateral project for scientific cooperation between the Republic of Slovenia and the State of Israel (NI-0002). S. Emin acknowledge the ARRS program P2-0412. M. Machrecki and T. Chouki acknowledge the scholarships provided by the Public Scholarship, Development, Disability and Maintenance Fund of the Republic of Slovenia (Ad futura program) for Ph.D. studies at the University of Nova Gorica. The authors acknowledge the textile company Tekstina d.o.o. (Ajdovščina, Slovenia) for providing us the B41 dye, which was used in the degradation studies.

## Appendix A. Supporting information

Supplementary data associated with this article can be found in the online version at [doi:10.1016/j.jece.2021.105495](https://doi.org/10.1016/j.jece.2021.105495).

## References

- [1] E. Kusmirek, Semiconductor electrode materials applied in photoelectrocatalytic wastewater treatment – an overview, *Catalysts* 10 (2020) 439, <https://doi.org/10.3390/catal10040439>.
- [2] S.W. Verbruggen, M. Van Hal, T. Bosserez, B. Hauchecorne, J. Rongé, B. Hauchecorne, J.A. Martens, S. Lenaerts, Harvesting hydrogen gas from air pollutants with an un-biased gas phase photo-electrochemical cell, *ChemSusChem* 10 (2017) 1413–1418, <https://doi.org/10.1002/cssc.201601806>.
- [3] P. Lianos, Production of electricity and hydrogen by photocatalytic degradation of organic wastes in a photoelectrochemical cell: the concept of the photofuelcell: a review of a re-emerging research field, *J. Hazard. Mater.* 185 (2011) 575–590, <https://doi.org/10.1016/j.jhazmat.2010.10.083>.
- [4] G.M. Peleyeju, E.H. Umukoro, J.O. Babalola, O.A. Arotiba, Solar-light-responsive titanium-sheet-based carbon nanoparticles/BiVO<sub>4</sub>/WO<sub>3</sub> photoanode for the photoelectrocatalytic degradation of orange II dye water pollutant, *ACS Omega* 5 (2020) 4743–4750, <https://doi.org/10.1021/acsomega.9b02148>.
- [5] J.B. Sambur, P. Chen, Distinguishing direct and indirect photoelectrocatalytic oxidation mechanisms using quantitative single-molecule reaction imaging and photocurrent measurements, *J. Phys. Chem. C* 120 (2016) 20668–20676, <https://doi.org/10.1021/acs.jpcc.6b01848>.
- [6] M.V.B. Zanoni, J.J. Sene, H. Selcuk, M.A. Anderson, Photoelectrocatalytic production of active chlorine on nanocrystalline titanium dioxide thin-film electrodes, *Environ. Sci. Technol.* 38 (2004) 3203–3208, <https://doi.org/10.1021/es0347080>.
- [7] M.S. Koo, X. Chen, K. Cho, T. An, W. Choi, X. Chen, K. Cho, T. An, W. Choi, In situ photoelectrochemical chloride activation using a WO<sub>3</sub> electrode for oxidative treatment with simultaneous H<sub>2</sub> evolution under visible light, *Environ. Sci. Technol.* 53 (2019) 9926–9936, <https://doi.org/10.1021/acs.est.9b02401>.
- [8] E. Brillas, C.A. Martínez-Huitle, Decontamination of wastewaters containing synthetic organic dyes by electrochemical methods. an updated review, *Appl. Catal. B* 166–167 (2015) 603–643, <https://doi.org/10.1016/j.apcatb.2014.11.016>.
- [9] I. Tantis, M. Antonopoulou, I. Konstantinou, P. Lianos, Coupling of electrochemical and photocatalytic technologies for accelerating degradation of organic pollutants, *J. Photochem. Photobiol. A Chem.* 317 (2016) 100–107, <https://doi.org/10.1016/j.jphotochem.2015.11.013>.
- [10] Y. Su, G.B. Wang, D.T.F. Kuo, M. Chang, Y. Shih, Photoelectrocatalytic degradation of the antibiotic sulfamethoxazole using TiO<sub>2</sub>/Ti photoanode, *Appl. Catal. B Environ.* 186 (2016) 184–192, <https://doi.org/10.1016/j.apcatb.2016.01.003>.
- [11] M.S. Koo, K. Cho, J. Yoon, W. Choi, Photoelectrochemical degradation of organic compounds coupled with molecular hydrogen generation using electrochromic TiO<sub>2</sub> nanotube arrays, *Environ. Sci. Technol.* 51 (2017) 6590–6598, <https://doi.org/10.1021/acs.est.7b00774>.
- [12] L. Osiewala, A. Socha, A. Perek, M. Socha, J. Rynkowski, Electrochemical, photochemical, and photoelectrochemical treatment of sodium p-cumenesulfonate, *Water Air Soil Pollut.* 224 (2013) 1657, <https://doi.org/10.1007/s11270-013-1657-3>.
- [13] G. Zhang, G. Huang, C. Yang, S. Chen, Y. Xu, S. Zhang, P. Lu, J. Sun, Y. Zhu, D. Yang, Efficient photoelectrocatalytic degradation of tylosin on TiO<sub>2</sub> nanotube arrays with tunable phosphorus dopants, *J. Environ. Chem. Eng.* 9 (2021), 104742, <https://doi.org/10.1016/j.jece.2020.104742>.
- [14] A.J. Cowan, W. Leng, P.R.F. Barnes, D.R. Klug, J.R. Durrant, Charge carrier separation in nanostructured TiO<sub>2</sub> photoelectrodes for water Splitting, *Phys. Chem. Chem. Phys.* 15 (2013) 8772–8778, <https://doi.org/10.1039/c3cp50318f>.
- [15] B.O. Orimolade, O.A. Arotiba, Towards visible light driven photoelectrocatalysis for water treatment: application of a FTO/BiVO<sub>4</sub>/Ag<sub>2</sub>S heterojunction anode for the removal of emerging pharmaceutical pollutants, *Sci. Rep.* 10 (2020) 1–13, <https://doi.org/10.1038/s41598-020-62425-w>.
- [16] M. Zhang, W. Pu, S. Pan, O.K. Okoth, C. Yang, J. Zhang, Photoelectrocatalytic activity of liquid phase deposited  $\alpha$ -Fe<sub>2</sub>O<sub>3</sub> films under visible light illumination, *J. Alloy. Compd.* 648 (2015) 719–725, <https://doi.org/10.1016/j.jallcom.2015.07.026>.
- [17] Q. Zeng, J. Bai, J. Li, L. Xia, K. Huang, X. Li, B. Zhou, A novel in situ preparation method for nanostructured  $\alpha$ -Fe<sub>2</sub>O<sub>3</sub> films from electrodeposited Fe films for efficient photoelectrocatalytic water splitting and the degradation of organic pollutants, *J. Mater. Chem. A* 3 (2015) 4345–4353, <https://doi.org/10.1039/c4ta06017b>.
- [18] Z. Zhang, F. Hossain, T. Takahashi, Self-assembled hematite ( $\alpha$ -Fe<sub>2</sub>O<sub>3</sub>) nanotube arrays for photoelectrocatalytic degradation of azo dye under simulated solar light irradiation, *Appl. Catal. B Environ.* 95 (2010) 423–429, <https://doi.org/10.1016/j.apcatb.2010.01.022>.
- [19] L. Cheng, L. Liu, R. Li, J. Zhang, Liquid phase deposition of  $\alpha$ -Fe<sub>2</sub>O<sub>3</sub>/ZnO heterojunction film with enhanced visible-light photoelectrocatalytic activity for pollutant removal, *J. Electrochem. Soc.* 164 (2017) 726–733, <https://doi.org/10.1149/2.0241712jes>.
- [20] L. Cheng, Y. Tian, J. Zhang, Construction of p-n heterojunction film of Cu<sub>2</sub>O/ $\alpha$ -Fe<sub>2</sub>O<sub>3</sub> for efficiently photoelectrocatalytic degradation of oxytetracycline, *J. Colloid Interface Sci.* 526 (2018) 470–479, <https://doi.org/10.1016/j.jcis.2018.04.106>.
- [21] R.D. Suryavanshi, S.V. Mohite, S.V. Shaikh, J.B. Thorat, K.Y. Rajpure, Spray deposited Fe<sub>2</sub>O<sub>3</sub> photoelectrode for degradation of benzoic acid and methyl blue dye under solar radiation, *J. Mater. Sci. Mater. Electron.* 29 (2018) 20875–20884, <https://doi.org/10.1007/s10854-018-0230-7>.
- [22] M. Mahadik, S. Shinde, V. Mohite, S. Kumbhar, K. Rajpure, A. Moholkar, J. Kim, C. Bhosale, Photoelectrocatalytic oxidation of rhodamine B with sprayed  $\alpha$ -Fe<sub>2</sub>O<sub>3</sub> photocatalyst, *Mater. Express* 3 (2013) 247–255, <https://doi.org/10.1166/mex.2013.1120>.
- [23] S. Garcia-Segura, E. Brillas, Applied photoelectrocatalysis on the degradation of organic pollutants in wastewaters, *J. Photochem. Photobiol. C Photochem. Rev.* 31 (2017) 1–35, <https://doi.org/10.1016/j.jphotochemrev.2017.01.005>.
- [24] M. Mishra, D.M. Chun,  $\alpha$ -Fe<sub>2</sub>O<sub>3</sub> as a photocatalytic material: a review, *Appl. Catal. A Gen.* 498 (2015) 126–141, <https://doi.org/10.1016/j.apcata.2015.03.023>.
- [25] S. Emin, M. De Respinis, T. Mavrić, B. Dam, M. Valant, W.A. Smith, Photoelectrochemical water splitting with porous  $\alpha$ -Fe<sub>2</sub>O<sub>3</sub> thin films prepared from Fe/Fe-Oxide nanoparticles, *Appl. Catal. A Gen.* 523 (2016) 130–138, <https://doi.org/10.1016/j.apcata.2016.06.007>.
- [26] A. Annamalai, P.S. Shinde, A. Subramanian, J.Y. Kim, S.H. Choi, J.S. Lee, J.S. Jang, Bifunctional TiO<sub>2</sub> underlayer for  $\alpha$ -Fe<sub>2</sub>O<sub>3</sub> nanorod based photoelectrochemical cells: enhanced interface and Ti<sup>4+</sup> doping, *J. Mater. Chem. A* 3 (2015) 5007–5013, <https://doi.org/10.1039/c4ta06315e>.
- [27] Y.S. Hu, A. Kleiman-shwarsstein, A.J. Forman, D. Hazen, J. Park, E.W. McFarland, Pt-doped  $\alpha$ -Fe<sub>2</sub>O<sub>3</sub> thin films active for photoelectrochemical water splitting, *Chem. Mater.* 20 (2008) 3803–3805, <https://doi.org/10.1021/cm800144q>.
- [28] L. Wang, C.Y. Lee, P. Schmuki, Ti and Sn co-doped anodic  $\alpha$ -Fe<sub>2</sub>O<sub>3</sub> films for efficient water splitting, *Electrochem. Commun.* 30 (2013) 21–25, <https://doi.org/10.1016/j.elecom.2013.01.013>.
- [29] M. Tadic, D. Trpkov, L. Kopanja, S. Vojnovic, M. Panjan, Hydrothermal synthesis of hematite ( $\alpha$ -Fe<sub>2</sub>O<sub>3</sub>) nanoparticle forms: synthesis conditions, structure, particle shape analysis, cytotoxicity and magnetic properties, *J. Alloy. Compd.* 792 (2019) 599–609, <https://doi.org/10.1016/j.jallcom.2019.03.414>.
- [30] Q. Meng, Z. Wang, X. Chai, Z. Weng, R. Ding, L. Dong, Fabrication of hematite ( $\alpha$ -Fe<sub>2</sub>O<sub>3</sub>) nanoparticles using electrochemical deposition, *Appl. Surf. Sci.* 368 (2016) 303–308, <https://doi.org/10.1016/j.apsusc.2016.02.007>.
- [31] C. Park, J. Walker, R. Tannenbaum, A.E. Stiegman, J. Frydrych, L. Machala, Sol-gel-derived iron oxide thin films on silicon: surface properties and interfacial chemistry, *ACS Appl. Mater. Interfaces* 1 (2009) 1843–1846, <https://doi.org/10.1021/am900362x>.
- [32] J.R. Avila, D.W. Kim, M. Rimoldi, O.K. Farha, J.T. Hupp, Fabrication of thin films of  $\alpha$ -Fe<sub>2</sub>O<sub>3</sub> via atomic layer deposition using iron disamidate and water under mild growth conditions, *ACS Appl. Mater. Interfaces* 7 (2015) 16138–16142, <https://doi.org/10.1021/acsami.5b04043>.
- [33] F. Le Formal, N. Tétreault, M. Cornuz, T. Moehl, M. Grätzel, K. Sivula, Passivating surface states on water splitting hematite photoanodes with alumina overlayers, *Chem. Sci.* 2 (2011) 737–743, <https://doi.org/10.1039/c0sc00578a>.
- [34] Y. Zhang, Y. Zhu, C. Lv, S. Lai, W. Xu, Enhanced visible-light photoelectrochemical performance via chemical vapor deposition of Fe<sub>2</sub>O<sub>3</sub> on a WO<sub>3</sub> film to form a heterojunction, *Rare Met.* 39 (2020) 841–849, <https://doi.org/10.1007/s12598-019-01311-5>.
- [35] S. Park, S. Lim, H. Choi, Chemical vapor deposition of iron and iron oxide thin films from Fe(II) dihydride complexes, *Chem. Mater.* 18 (2006) 5150–5152, <https://doi.org/10.1021/cm0601990>.
- [36] D. Peeters, A. Sadlo, K. Lowjaga, O. Mendoza Reyes, L. Wang, L. Mai, M. Gebhard, D. Rogalla, H.W. Becker, I. Giner, G. Grundmeier, D. Mitoraj, M. Grafen, A. Ostendorf, R. Beranek, A. Devi, Nanostructured Fe<sub>2</sub>O<sub>3</sub> processing via water-assisted ALD and low-temperature CVD from a versatile iron ketoiminate



- precursor, *Adv. Mater. Interfaces* 4 (2017), 1700155, <https://doi.org/10.1002/admi.201700155>.
- [37] Z.H. Barber, The control of thin film deposition and recent developments in oxide film growth, *J. Mater. Chem.* 16 (2006) 334–344, <https://doi.org/10.1039/B506228D>.
- [38] S.C. Riha, J.M. Racowski, M.P. Lanci, J.A. Klug, A.S. Hock, A.B.F. Martinson, Phase discrimination through oxidant selection in low-temperature atomic layer deposition of crystalline iron oxides, *Langmuir* 29 (2013) 3439–3445, <https://doi.org/10.1021/la305027k>.
- [39] A.B.F. Martinson, M.J. Devries, J.A. Libera, S.T. Christensen, J.T. Hupp, M.J. Pellin, J.W. Elam, Atomic layer deposition of  $\text{Fe}_2\text{O}_3$  using ferrocene and ozone, *J. Phys. Chem. C* 115 (2011) 4333–4339, <https://doi.org/10.1021/jp110203x>.
- [40] A. Tamm, M.C. Dimri, J. Kozlova, A. Aidla, T. Tätt, T. Arroval, U. Mäeorg, H. Mändar, R. Stern, K. Kukli, Atomic layer deposition of ferromagnetic iron oxide films on three-dimensional substrates with tin oxide nanoparticles, *J. Cryst. Growth* 343 (2012) 21–27, <https://doi.org/10.1016/j.jcrysgro.2011.09.062>.
- [41] X. Deng, H. Tüysüz, Cobalt-oxide-based materials as water oxidation catalyst: recent progress and challenges, *ACS Catal.* 4 (2014) 3701–3714, <https://doi.org/10.1021/cs500713d>.
- [42] M. Shandilya, R. Rai, J. Singh, M. Shandilya, R. Rai, J. Singh, Review: hydrothermal technology for smart materials, *Adv. Appl. Ceram.* 115 (2016) 354–376, <https://doi.org/10.1080/17436753.2016.1157131>.
- [43] M.D.A. Tyona, Theoretical study on spin coating technique, *Adv. Mater. Res.* 2 (2013) 195–208, <https://doi.org/10.12989/amr.2013.2.4.195>.
- [44] T. Chouki, M. Machrecki, S. Emin, Solvothermal synthesis of iron phosphides and their application for efficient electrocatalytic hydrogen evolution, *Int. J. Hydrog. Energy* 45 (2020) 21473–21482, <https://doi.org/10.1016/j.ijhydene.2020.05.257>.
- [45] A.E. Müftüoglu, B. Karakelle, M. Ergin, A.Y. Erkol, F. Yilmaz, The removal of basic blue 41 dye from aqueous solutions by bituminous shale, *Adsorpt. Sci. Technol.* 21 (2003) 751–760, <https://doi.org/10.1260/026361703773581803>.
- [46] Y. Yin, X. Zhang, C. Sun, Transition-metal-doped  $\text{Fe}_2\text{O}_3$  nanoparticles for oxygen evolution reaction, *Prog. Nat. Sci. Mater. Int.* 28 (2018) 430–436, <https://doi.org/10.1016/j.pnsc.2018.07.005>.
- [47] K. Sivula, R. Zboril, F. Le Formal, R. Robert, A. Weidenkaff, J. Tucek, J. Frydrych, M. Grätzel, Photoelectrochemical water splitting with mesoporous hematite prepared by a solution-based colloidal approach, *J. Am. Chem. Soc.* 132 (2010) 7436–7444, <https://doi.org/10.1021/ja101564f>.
- [48] H. Zhang, J. Song, C. Liu, Immobilization of  $\alpha\text{-Fe}_2\text{O}_3$  nanoparticles on PET fiber by low temperature hydrothermal method, *Ind. Eng. Chem. Res.* 52 (2013) 7403–7412, <https://doi.org/10.1021/ie400019t>.
- [49] A.I. Inamdar, S.H. Mujawar, V. Ganesan, P.S. Patil, Surfactant-mediated growth of nanostructured zinc oxide thin films via electrodeposition and their photoelectrochemical performance, *Nanotechnology* 19 (2008), 325706, <https://doi.org/10.1088/0957-4484/19/32/325706>.
- [50] H. Uchiyama, K. Isobe, H. Kozuka, Preparation of porous  $\text{CuO}$  films from  $\text{Cu}(\text{NO}_3)_2$  aqueous solutions containing poly(vinylpyrrolidone) and their photocathodic properties, *RSC Adv.* 7 (2017) 18014–18018, <https://doi.org/10.1039/C6RA26590A>.
- [51] C. Zhu, C. Li, M. Zheng, J.J. Delaunay, Plasma-induced oxygen vacancies in ultrathin hematite nanoflakes promoting photoelectrochemical water oxidation, *ACS Appl. Mater. Interfaces* 7 (2015) 22355–22363, <https://doi.org/10.1021/acsami.5b06131>.
- [52] Y. Liang, C.S. Enache, R. Krol, Photoelectrochemical characterization of sprayed  $\alpha\text{-Fe}_2\text{O}_3$  thin films: influence of Si doping and  $\text{SnO}_2$  interfacial layer, *Int. J. Photo* 2008 (2007) 1–7, <https://doi.org/10.1155/2008/739864>.
- [53] K. Gelderman, L. Lee, S.W. Donne, Flat-band potential of a semiconductor: using the mott–schottky equation, *J. Chem. Educ.* 84 (2007) 685–688, <https://doi.org/10.1021/ed084p685>.
- [54] A. Annamalai, P.S. Shinde, T.H. Jeon, H.H. Lee, H.G. Kim, W. Choi, J.S. Jang, Fabrication of superior  $\alpha\text{-Fe}_2\text{O}_3$  nanorod photoanodes through ex-situ Sn-doping for solar water splitting, *Sol. Energy Mater. Sol. Cells* 144 (2016) 247–255, <https://doi.org/10.1016/j.solmat.2015.09.016>.
- [55] C. Lu, P.R. Jothi, T. Thersleff, T.M. Budnyak, A. Rokicinska, K. Yubuta, R. Dronskowski, P. Kuśrowski, B.P.T. Fokwa, A. Slabon, Nanostructured core-shell metal borides-oxides as highly efficient electrocatalysts for photoelectrochemical water oxidation, *Nanoscale* 12 (2020) 3121–3128, <https://doi.org/10.1039/C9NR09818F>.
- [56] Y. Hu, Y. Wu, J. Feng, H. Huang, C. Zhang, Q. Qian, T. Fang, J. Xu, P. Wang, Z. Li, Z. Zouac, Rational design of electrocatalysts for simultaneously promoting bulk charge separation and surface charge transfer in solar water splitting photoelectrodes, *J. Mater. Chem. A* 6 (2018) 2568–2576, <https://doi.org/10.1039/C7TA10361A>.
- [57] Y.H. Wu, T. Wu, Y.W. Lin, Photoelectrocatalytic degradation of methylene blue on cadmium sulfide-sensitized titanium dioxide film, *Mater. Res. Bull.* 118 (2019), 110500, <https://doi.org/10.1016/j.matresbull.2019.110500>.
- [58] Y.M. Hunge, Photoelectrocatalytic degradation of 4-chlorophenol using nanostructured  $\alpha\text{-Fe}_2\text{O}_3$  thin films under sunlight illumination, *J. Mater. Sci. Mater. Electron* 15 (2017) 11260–11267, <https://doi.org/10.1007/s10854-017-6915-5>.
- [59] R. Brüninghoff, A.K. Van Duijne, L. Braakhuis, P. Saha, A.W. Jeremiasse, B. Mei, G. Mul, Comparative analysis of photocatalytic and electrochemical degradation of 4-ethylphenol in saline conditions, *Environ. Sci. Technol.* 53 (2019) 8725–8735, <https://doi.org/10.1021/acs.est.9b01244>.
- [60] S. Iguchi, Y. Miseki, K. Sayama, Efficient hypochlorous acid (HClO) production: via photoelectrochemical solar energy conversion using a  $\text{BiVO}_4$ -based photoanode, *Sustain. Energy Fuels* 2 (2018) 155–162, <https://doi.org/10.1039/c7se00453b>.
- [61] J. Staehelin, J. Hoigne, Decomposition of ozone in water in the presence of organic solutes acting as promoters and inhibitors of radical chain reactions, *Environ. Sci. Technol.* 19 (1985) 1206–1213, <https://doi.org/10.1021/es00142a012>.
- [62] K. Cho, Y. Qu, D. Kwon, H. Zhang, C.A. Cid, A. Aryanfar, M.R. Hoffman, Effects of anodic potential and chloride ion on overall reactivity in electrochemical reactors designed for solar-powered wastewater treatment, *Environ. Sci. Technol.* 48 (2014) 2377–2384, <https://doi.org/10.1021/es404137u>.
- [63] J. Zhang, J. Zheng, W. Yang, Co-degradation of ammonia nitrogen and 4-chlorophenol in a photoelectrochemical system by a tandem reaction of chlorine and hydroxyl radicals, *Chem. Eng. Sci.* 226 (2020), 115813, <https://doi.org/10.1016/j.ces.2020.115813>.
- [64] Y. Ji, J. Bai, J. Li, T. Luo, L. Qiao, Q. Zeng, B. Zhou, Highly selective transformation of ammonia nitrogen to  $\text{N}_2$  based on a novel solar-driven photoelectrocatalytic-chlorine radical reactions system, *Water Res.* 125 (2017) 512–519, <https://doi.org/10.1016/j.watres.2017.08.053>.
- [65] Y. Zhang, Y. Ji, J. Li, J. Bai, S. Chen, L. Li, J. Wang, T. Zhou, P. Jiang, X. Guan, B. Zhou, Efficient ammonia removal and toxic chlorate control by using  $\text{BiVO}_4/\text{WO}_3$  heterojunction photoanode in a self-driven PEC-chlorine system, *J. Hazard. Mater.* 402 (2021), 123725, <https://doi.org/10.1016/j.jhazmat.2020.123725>.
- [66] H. Park, C.D. Vecitis, M.R. Hoffmann, Electrochemical water splitting coupled with organic compound oxidation: the role of active chlorine species, *J. Phys. Chem. C* 113 (2009) 7935–7945, <https://doi.org/10.1021/jp810331w>.
- [67] X.Y. Yu, Z.C. Bao, J.R. Barker, Free radical reactions involving  $\text{Cl}^\bullet$ ,  $\text{Cl}_2^\bullet$ , and  $\text{SO}_4^\bullet$  in the 248 nm photolysis of aqueous solutions containing  $\text{S}_2\text{O}_8^{2-}$  and  $\text{Cl}^-$ , *J. Phys. Chem. A* 108 (2004) 295–308, <https://doi.org/10.1021/jp036211i>.
- [68] H. Wang, X. Zhang, Y. Su, H. Yu, S. Chen, X. Quan, F. Yang, Photoelectrocatalytic oxidation of aqueous ammonia using  $\text{TiO}_2$  nanotube arrays, *Appl. Surf. Sci.* 311 (2014) 851–857, <https://doi.org/10.1016/j.apsusc.2014.05.195>.
- [69] M. Heipel, J. Luo, Photoelectrochemical mineralization of textile diazo dye pollutants using nanocrystalline  $\text{WO}_3$  electrodes, *Electrochim. Acta* 47 (2001) 729–740, [https://doi.org/10.1016/S0013-4686\(01\)00753-8](https://doi.org/10.1016/S0013-4686(01)00753-8).
- [70] J. Luo, M. Heipel, Photoelectrochemical degradation of naphthol blue black diazo dye on  $\text{WO}_3$  film electrode, *Electrochim. Acta* 46 (2001) 2913–2922, [https://doi.org/10.1016/S0013-4686\(01\)00503-5](https://doi.org/10.1016/S0013-4686(01)00503-5).
- [71] K. Prakash, J.V. Kumar, P. Latha, P.S. Kumar, S. Karuthapandian, Fruitful fabrication of CDs on GO/g- $\text{C}_3\text{N}_4$  sheets layers: a carbon amalgamation for the remediation of carcinogenic pollutants, *J. Photochem. Photobiol. A Chem.* 370 (2019) 94–104, <https://doi.org/10.1016/j.jphotochem.2018.10.046>.
- [72] M. Heipel, S. Hazelton, Photoelectrocatalytic degradation of diazo dyes on nanostructured  $\text{WO}_3$  electrodes, *Electrochim. Acta* 50 (2005) 5278–5291, <https://doi.org/10.1016/j.electacta.2005.03.067>.
- [73] B.N. Grgur, D.Z. Mijin, A kinetics study of the methomyl electrochemical degradation in the chloride containing solutions, *Appl. Catal. B Environ.* 147 (2014) 429–438, <https://doi.org/10.1016/j.apcatb.2013.09.028>.
- [74] S. Ferro, A. De Battisti, Electrocatalysis and chlorine evolution reaction at ruthenium dioxide deposited on conductive diamond, *J. Phys. Chem. B* 106 (2002) 2249–2254, <https://doi.org/10.1021/jp012195i>.
- [75] R. Yuan, S.N. Ramjaun, Z. Wang, J. Liu, Effects of chloride ion on degradation of acid orange 7 by sulfate radical-based advanced oxidation process: implications for formation of chlorinated aromatic compounds, *J. Hazard. Mater.* 196 (2011) 173–179, <https://doi.org/10.1016/j.jhazmat.2011.09.007>.
- [76] H. Zeghio, N. Khellaf, A. Amrane, H. Djelal, M. Bouhelassa, A.A. Assadi, S. Rtimi, Combining photocatalytic process and biological treatment for Reactive Green 12 degradation: optimization, mineralization, and phytotoxicity with seed germination, *Environ. Sci. Pollut. Res.* 28 (2021) 12490–12499, <https://doi.org/10.1007/s11356-020-11282-1>.
- [77] I. Olvera-Rodríguez, R. Hernández, A. Medel, C. Guzmán, L. Escobar-Alarcón, E. Brillás, I. Sirés, K. Esquivel,  $\text{TiO}_2/\text{Au}/\text{TiO}_2$  multilayer thin-film photoanodes synthesized by pulsed laser deposition for photoelectrochemical degradation of organic pollutants, *Sep. Purif. Technol.* 224 (2019) 189–198, <https://doi.org/10.1016/j.seppur.2019.05.020>.
- [78] S. Ghosh, N.A. Kouame, S. Remita, L. Ramos, F. Goubard, P.H. Aubert, A. Dazzi, A. Deniset-Besseau, H. Remita, Visible-light active conducting polymer nanostructures with superior photocatalytic activity, *Sci. Rep.* 5 (2015) 1–9, <https://doi.org/10.1038/srep18002>.
- [79] L. Mu, Z. He, X. Kong, C. Liang, Y. Wang, A. Danel, E. Kulig, G.H.W. Milburn, Towards color stable blue primary for displays: suppress field-dependent color change in a multilayered electroluminescent device, *J. Disp. Technol.* 7 (2011) 96–104, <https://doi.org/10.1109/JDT.2010.2096532>.